

POLYTECHNIC OF TURIN

Master's Degree in Aerospace Engineering



OPTIMAL PLACEMENT OF A PIEZOELECTRIC SENSOR EMBEDDED IN A SMART STRUCTURE: ANALYTICAL EVALUATION AND TECHNOLOGICAL PROCEDURE

Supervisors:

Prof. Giacomo Frulla

Prof. Enrico Cestino

Candidate

Sami Khreisat

2019/2020

PURDUE UNIVERSITY



External Supervisor:

Dr. James M. Gibert

College of Engineering
School of Mechanical Engineering
Ray W. Herrick Laboratories

ACKNOWLEDGEMENTS

I want to express my gratitude to my external advisors, Dr. James M. Gibert, for his patience and his guidance throughout this path. I would also like to thank Giacomo Frulla and Professor Enrico Cestino, for allowing me to research such an exciting topic in one of the best universities in the entire world. A special thank goes to Danzi Francesco and his exceptional help during every stage of my work. Without his help, I wouldn't be able to conclude my job and be where I am now and to Fabrizio Cicala, a true friend.

Contents

	List of Tables	ii
	List of Figures	iii
1	Introduction	1
	1.1 Smart materials Property Overview.....	1
	1.1.1 Piezoelectric Material Properties.....	1
	1.1.2 UAM Process Overview.....	3
	1.2 Thesis Objective.....	5
	1.4 Thesis Outline.....	5
2	Literature Review	6
3	Modal Frequencies and Shapes	8
	3.1 Electromechanical Euler-Bernoulli Model with Embedded Element.....	8
	3.1.1 Energy Expressions.....	11
	3.2 Governing Equations and Boundary Conditions.....	15
	3.3 Free Vibration.....	16
4	Dynamic Of The Model With Embedded PVDF Material Element	20
	4.1 Orthogonality of Normal Modes Euler-Bernoulli Model with Embedded Element.	20
	4.1.1 First Part of the Beam.....	20
	4.1.2 Second Part of the Beam.....	21
	4.1.3 Orthogonality of Normal Modes Solution.....	22
	4.2 Forced Vibration Problem.....	23
	4.2.1 First part of the Beam.....	23
	4.2.2 Second Beam.....	24
	4.2.3 Forced Vibration Solution.....	25
	4.3 FEA Model Description.....	27
	4.3.1 FEA Model Validation.....	29
5	Analytical Results	33
	5.1 PVDF Length Variation.....	33
	5.2 PVDF Layer Position.....	36
	5.3 PVDF Layer Thickness.....	38
	5.4 PVDF Young Modulus Variation.....	40
6	Conclusion and Future Work	43
	6.1 Summary.....	43
	6.2 Future Work.....	44
A	Appendix: Hamiltonian equation	46
B	Appendix: Coefficients of Constraint Equations	47
C	Appendix; Clamp Design Process	50

List of Tables

1	Material Properties and geometries of the analyzed beam.....	28
2	Comparison of modal frequency of the analytical solution and the FEA model for an Al3003 stepped beam.....	29
3	Comparison of modal frequencies of the analytical solution and FEA model for a composite cantilever Al3003/PVDF/Al3003 beam.....	32
4	Displacement result comparison of the analytical solution and the FEA model, composite cantilever Al3003/PVDF/Al3003 beam.....	32
5	Optimal configuration for a beam with a PVDF sensor embedded.....	43

List of Figures

1	Walked Alluminum tape detail.....	4
2	Displacement field for an Euler-Bernoulli beam with an embedded piezoelectric element, shown in gray.....	10
3	PATRAN model of the cantilever stepped beam with an embedded sensor used for the validation, lateral view.....	27
4	PATRAN model of the meshed cantilever stepped beam with an embedded sensor used for the validation, with base acceleration and constraints applied on the root.....	29
5	Modal shapes of Al3003 stepped beam: a), c), e), g), i) are analytical mode shapes, and b), d), f), h) and j) are the FEA mode shapes. The red line indicates beam section one and the black line indicates beam section two.....	30
6	Modal shapes of of composite beam: a), c), e), g), i) are analytical mode shapes, and b), d), f), h) and j) are the FEA mode shapes. The red line indicates beam section one and the black line indicates beam section two.....	31
7	PVDF length 3D analysis variation. X-axis = resistance variation, Y-axis =piezoelectric layer's length, Z-axis = piezoelectric voltage output.....	34
8	PVDF length-frequency of normal modes variation, 2D analysis, first frequency of normal modes variation with a fixed resistance of 8e8 [Ohm], X-axis = length of the first part of the beam Y-axis =first frequency of normal modes.....	34
9	PVDF length-frequency of normal modes variation, 2D analysis, first frequency of normal modes variation with a fixed resistance of 8e8 [Ohm], X-axis = length of the first part of the beam Y-axis =first frequency of normal modes.....	35
10	Piezoelectric layer Position variation, 3D analysis, X-axis = resistance variation, Y-axis =piezoelectric layer's length, Z-axis = piezoelectric voltage output.....	36
11	PVDF layer position-neutral axis variation, 2D analysis, X-axis = PVDF layer position, Y-axis =neutral axis position.....	37
12	PVDF position-frequency of normal modes variation, 2D analysis, first frequency of normal modes variation with a fixed resistance of 8e8 [Ohm], X-axis = PVDF position [m], Y-axis =first frequency of normal modes.....	37
13	PVDF position-voltage output variation with fixed resistance of 8e8 [Ohm] detail, 2D analysis, X-axis : PVDF layer position, Y-axis : piezoelectric material output tension.....	38
14	PVDF thickness variation, 3D analysis, X-axis = resistance variation, Y-axis = piezoelectric layer's thickness, Z-axis = piezoelectric voltage output.....	38
15	PVDF layer thickness-neutral axis variation, 2D analysis, X-axis = PVDF layer thickness, Y-axis = neutral axis position.....	39
16	PVDF layer thickness-voltage output variation with fixed resistance of 8e8 detail, 2D analysis, X-axis : PVDF layer thickness, Y-axis : piezoelectric material output tension.....	39
17	Young modulus- variation, 3D analysis, X-axis = resistance variation, Y-axis = $\frac{E_{material}}{E_{PVDF}}$, Z-axis = piezoelectric voltage output.....	40
18	Young modulus-neutral axis variation, 2D analysis, X-axis = $\frac{E_{material}}{E_{PVDF}}$, Y-axis = neutral axis position.....	41
19	Young modulus-frequency of normal modes variation, 2D analysis, first frequency of normal modes variation with a fixed resistance of 8e8 [Ohm], X-axis = $\frac{E_{material}}{E_{PVDF}}$, Y-axis = first frequency of normal modes.....	41
20	Young modulus-voltage output variation with fixed resistance of 8e8 [Ohm] detail, 2D analysis, X-axis : $\frac{E_{material}}{E_{PVDF}}$, Y-axis : piezoelectric material output tension.....	42

21	First Design Model, Upper view.....	51
22	Second design model, upper view.....	51
23	Second design model, screw driver detail.....	52
24	Third design model, upper view.....	53
25	Third design model, screw driver detail.....	53
26	Third design model test, upper view.....	54
27	Third design clamp model bending, lateral view.....	54
28	First test result, lateral view.....	55
29	Second test result, lateral view.....	56
30	Second test result, detail.....	56
31	Welding parameters, UAM machine display.....	57
32	Fourth design, cylinder support, lateral view, detail.....	58
33	Fourth Design, Cylinder, lateral view detail.....	59
34	Design, upper view.....	60
35	Sixth Design.....	60
36	Sixth Design, upper view.....	61

CHAPTER 1

INTRODUCTION

1.1 Smart Materials Property Overview

Smart materials are a new generation of materials with the general feature that environmental changing conditions can significantly influence their material properties. These materials can adapt to different stimuli, such as temperature, electrical and magnetic field, chemicals, pressure, and loads. The modification obtained of stiffness, damping, or shape of the smart materials can provide multiple functionalities of the material or its structure.

These materials are widely used for civil, mechanical, aerospace, mechatronics, biomedical, and energetic purposes because they can detect changes in the environment (using them as sensors), or be controlled by modifying some outside conditions (using them as actuators).

Smart materials can be classified in three different way:

- 1) Type of material response: it can be active or passive
- 2) Modifications obtained: geometrical or chemical-physical
- 3) Type of magnetic field involved: electrical, thermal, or magnetic

In this dissertation, piezoelectric smart materials will be used and studied to develop an analytical framework to understand embedded sensors and energy harvesting devices' behavior. They will be embedded because the embedding will protect them from harsh environments.

1.1.1 Piezoelectric Material Properties

Piezoelectricity is the properties of some particular materials to convert mechanical stress or strain into electrical energy due to the crystal lattice's polarization and, at the same time, if they are exposed to an electrical field, they are affected by elastic deformation.

Piezoelectricity has two different properties:

1. Direct piezoelectric effect: the application of mechanical forces to the material is converted into electrical potential, so there is a voltage output from the material.
2. Inverse piezoelectric effect: applying an external electric field to the material produces a reorganization of the crystal inside the piezoelectric material that becomes an elastic deformation.

So, the process itself is reversible.

These type of materials are ruled by two constitutive equations

$$D_i = \varepsilon_{ij}E_j + d_{ijk}\sigma_{jk} \quad 1.1$$

$$e_{ij} = d_{kij}E_k + C_{ijkl}\sigma_{kl} \quad 1.2$$

Where D_i is the electric displacement, ϵ_{ij} is the permittivity of the material, E_j and E_k are the electrical field, d_{ijk} represents the direct piezoelectric and σ_{jk} and σ_{kl} are the mechanical stress, and C_{ijkl} is the mechanical compliance.

In order to better understand the piezoelectricity effect, it is necessary to understand the concept of dielectric materials. Piezoelectric materials, such as quartz, are a particular type of anisotropic dielectrics materials. These type of material don't have a cristal symmetric center, and when they are exposed to an electrical field or are loaded with other methods, the electrical dipoles appear (an electro-neutral unit of volume made by two opposite and equal charges separated by a finite distance), and they align with it making the reticular crystal asymmetric. This mechanism's results are the polarization of the material, which is the total moment dipole for a unit of volume.

$$P = \frac{1}{V} \sum_i \mu_i \quad 1.3$$

The other type of piezoelectric materials (e.g. quartz) are pyroelectric (e.g. ZnO), and ferroelectric (e.g. PZT, PMN-PT, PVDF).

Pyroelectricity is a property that some materials have, and it is a subcategory of the piezoelectric materials. This property allows the material to change their polarization if heat sources are applied to it or vice-versa.

The last subcategory of materials that are considered piezoelectric is the one that will be studied and used in this work, the ferroelectric materials.

These materials are crystal with a high dielectric constant that allows them to hold their polarization even after the electric field is removed.

The main characteristic of these class of materials are:

1. The presence of a hysteresis circle polarization-electrical field.
2. Residual polarization also without an electrical field.
3. After a specific temperature T_c (Curie temperature), they become paraelectric materials.
4. After one particular point, they present saturation of the polarization. Even if a huger electrical field is applied, the polarization will not increase
5. They present Weiss domains in different directions.

1.1.2 UAM Process Overview

The Ultrasonic consolidation is an innovative technology patented by Dawn White in 1999. Solidica Inc commercialized it, and now, this technology belongs to Fabrisonic Inc.

Ultrasonic consolidation (UC), also known as Ultrasonic Additive Manufacturing (UAM), is an emerging solid-state technique that allows the formation of three-dimensional objects by ultrasonically joining, layer by layer, foils of similar and dissimilar metals for embedded objects, to form a solid part. It mainly differs from other technologies because it creates a joining without melting between two metals, and it works with low temperatures.

The main advantage of this technology are:

- An atmosphere control is not required during the process.
- Due to the low temperature of the process, less energy is required.
- Distortion and residual stresses are reduced because of the micro-friction process.
- Uniform composition without adhesive or fillers, integration of a wide variety of components, such as fibers and electronics, into a solid-state matrix.

Although these advantages, the UC operation shows critical welding failure issues as the height of the built feature increases and is related to the tape walking. As shown in the figure--, the walking problem could be a severe problem. The tape can move during the bonding process with the component's loss, but the reasons for this problem are not bright yet.

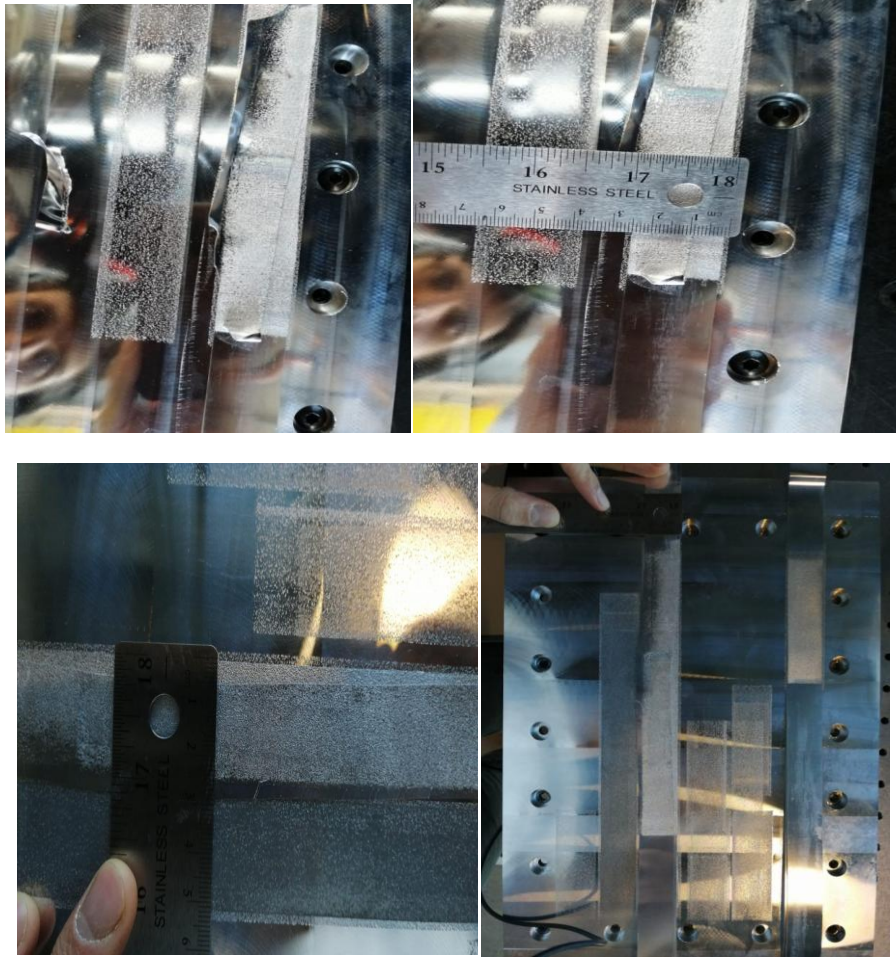


Figure 1: Walked Aluminum tape detail

Regarding the height of the structure, there is the "height to width ratio problem" (Robinson, Zhang, and Ram 2006). When the width of the structure is almost its height feature, bonding failure occurs, height feature, bonding failure occurs.

In order to understand this work, a comprehensive understanding of the welding process, the machine, and the bonding process is required.

Figure -- shows an overview of the UC process. The UAM process begins with the placement of a layer of a thin metal foil on a sacrificial baseplate. Then the vibrations generated by the piezoelectric device, which vibrates at a frequency of 20 kHz with an amplitude range between 5 and 40 μm , are transmitted by a circular rolling Sonotrode, which is pressed against the foil with a load from 50 to 1600 N. The transverse motion imparted to the top of the tape creates a friction action between the baseplate and the foil. This action induces a motion between the foil and the baseplate to shear surface asperities and disperses surface oxides. The high-frequency transverse vibration results in a shear deformation between the baseplate and the foil. This process induces grain growth and dynamic recrystallization across the surface that ends with micro welds at the bonding interface.

When the bonding of a layer is completed, additional layers are deposited to create a substrate and welded with the same procedure. After a layer deposition is welded, the subtractive step, with a

computer numerical control (CNC) milling machining, is started. The CNC milling head is used to shape the deposition in order to produce a 3D metal structure. This whole process is repeated until the desired dimensions of the structure are reached.

Along with selective laser sintering (SLS), an additive manufacturing process that allows to sinter powder creating 3D objects, UAM is one mechanism to embed smart materials in structures. The UAM technique was chosen because of his particular characteristic that allows embedding smart materials at room temperature and doesn't affect the embedded material.

1.2 Thesis Objective

The objective of this chapter is to explain the concept of this work and his development.

This dissertation has given an analytical framework that allows to understand what can happen if a piezoelectric sensor is inside of a beam and how the position, length, and thickness can impact the beam's behavior on different aspects and the harvested electrical power.

1.3 Thesis Outline

The manuscript is organized as follows:

Chapter one: A brief overview on UAM (ultrasonic additive manufacturing) process and an introduction of the piezoelectric materials properties followed by the research motivation and objective.

Chapter two: A review of all the relevant literature that allows the realization of this dissertation.

Chapter three: An analytical study of the governing equations of motion and electrical behavior of an Al3003/PVDF/Al3003 beam and an analytical analysis of the free vibration problem..

Chapter four: A dynamic study of the structure considered in chapter three followed by a description of the FEA model used to validate the analytical analysis done

Chapter five: A parametric 3D analysis based on the variation of geometric properties of the piezoelectric material considerate and the variation of the resistance of the equivalent circuit considered is presented in order to understand how the variation of these variables affect the beam behavior.

Chapter six: Provides results and suggested direction for future works

CHAPTER 2

LITERATURE REVIEW

In this chapter, a literature review of energy harvesting and stepped beam analysis has been presented.

Piezoelectric materials were used and studied in many ways due to their low cost, versatility, and capacity to transform energy from the external system and transform it into electrical power. Researchers have used many methods and several types of analysis in order to study, improve, and control the harvesting process. Tiersten [23], in his work, deeply studied a way to use Hamilton's principle to describe the piezoelectric physical effect mathematically valid for a linear piezoelectric material, using the variational principle. This principle was used to obtain approximated boundary conditions and governing equations that can be solved precisely. Henry A. Soldano, Daniel J. Inman, and Gyuhae Park [11], and Rames Chandra and Inderjit Choprat [] showed and described the various harvesting power effect, their behavior, and their applications as sensors and actuators in different structures such as beams and plates. To be exact, Henry A. Soldano, Daniel J. Inman, and Gyuhae Park [12] made a review on the power harvesting of the piezoelectric devices describing the fundamentals of this process, the efficiency of this phenomena, and every aspect related to it such as the storage mechanism and the circuitry related and the damping effect of the power harvesting.

Many investigation were made to optimize the location on a surface of a piezoelectric material in a smart structure and control specific natural behavior of the beam, Crawley and de Luis [5] focused on using the piezoelectric materials as actuators in intelligent structures. These authors developed static and dynamic analytical models. Then, they bonded piezoelectric materials to a substructure and in laminated structures to show the effectiveness of this materials actuator. Then, they found the position to maximize the moments and the modal forces of a system, Barboni et al. [2], Ip and Tse [14] Quек et al. [21] found the optimal length position to maximize the deflection of the structure. Barboni et al. [2] found that a criterion that allows finding the best length position for actuators could be the dynamic deflection in the case of a cantilever beam. This method will enable them to understand that the optimal placement is placed between two consecutive points on the beam, where the curvature is equal to zero. Ip and Tse [14] discovered that it would obtain the maximum efficiency if the sensor is placed at the antinodes of the fourth and the fifth nodes modes, while Quек et al. [] worked on the study of a sensor that can control the first and the second modes of the normal modes simultaneously. Wang and Wang [24], and 'Peng et al.[16] found the position to maximize the controllability degree, and Moheimani and Ryall [18] Maximized the degree of the modal controllability.

As regards the stepped beam analysis, D.C.D. Oguamanam and J.S. Hansen [6] and Francesco Danzi, and James Gibert [9] worked on an analytical study of an Euler-Bernoulli stepped beam whit a piezoelectric element for harvesting and sensing purposes. Oguamanam [6] studied a stepped beam structure with an arbitrary angle between the two sections of the beams and a tip mass at the end of the second part. The authors presented a complete and detailed analytical study focusing on the governing equation of the motion, free vibration analysis, and the orthogonality condition of this type of structure. On the other hand, Danzi [9] studied an angle-shaped resonator composed of two beams attached with different angle configurations. The writers focused on the mathematical

derivation for the system's dynamic and the electro-mechanical equation that rules the angle-shaped resonator's motion and compared the analytical solution founded with a semi-analytical solution using a FEA model.

Reviewing the literature finds that nobody studied what would happen using a single eccentric layer of PVDF and the optimal parameters that allows to find the optimal harvesting power output related to them. In the next sections an analytical study of a cantilever stepped beam with a piezoelectric embedded layer will be showed.

CHAPTER 3

MODAL FREQUENCIES AND SHAPES

In this chapter an analytical framework is developed for modelling an Euler Bernoulli beam with an embedded piezoelectric element. The goal is to determine the modal frequencies and modal shapes that can be used in the Chapter 4 to develop analytical solutions to the forced vibration analysis. The beam is multifunctional in that the embedded element can be used as a sensor, energy harvester or as a means to control unwanted oscillations or a large amplitude response.

The chapter begins by presenting the assumptions that were made during the formulation of the framework, the derivation of the motion equations of the beam, and the determination of the modal shapes and frequencies of the system. A linear constitutive relationship for both the piezoelectric and structural elements was used, and the whole structure was considered as an isotropic material. The Extended Hamilton's principle along with Kirchhoff's Voltage Law are used to derive the differential equations that govern the electrical and the mechanical behaviour of this structure.

3.1 Electromechanical Euler-Bernoulli Model with Embedded Element

Figure 2 depicts the model considered for this analysis. This system is composed of a metal with an embedded piezoelectric element placed near the base of the beam and can be modelled as two separate beams, a composite connected to a homogenous beam. The first beam's origin is at the base and extends to the end of the piezoelectric element. The section has length l , modulus E_b , width b , height $h_1 + h_3$, and a mass density ρ_b . The latter starts from the end of the first beam to the end of the entire structure and has length L , modulus E_b , width b , height $h_1 + h_2 + h_3$, and mass density ρ_b . Similarly, the piezoelectric element embedded in the structure has length l , modulus E_p , width b , height h_2 , and density ρ_p electromechanical coupling constant e_{31} and permittivity ϵ_{33} .

In Euler-Bernoulli beam or thin beam theory, the cross-section of the beam is not affected by deformation under transverse or axial load. Additionally, the cross-section of the beam remains normal and planar with respect to the deformed axis of the beam during the deformation. This is shown in Figure 2 by the lack of distortion in line segments BA and CD after bending to yield BA' and CD' . It is important to note that neutral axis varies along the length of the beam. Note that two materials cause the first beam's neutral axis to be shifted from the beam's geometric center. The position can be obtained using axial equilibrium and assuming the strain is continuous across the cross section of the beam while the stress is discontinuous. The resulting location of the neutral axis can be written as

$$Z_n = \frac{E_b(h_1^2 + h_3^2) + E_p h_2^2 + 2E_b(h_1 h_3 + h_2 h_3) + 2E_p h_1 h_2}{2E_b(h_1 + h_3) + 2E_p h_2}, \quad (3.1)$$

for the first beam and $Z_n = h/2$ for the second beam. Note that the analysis of the system requires two fixed coordinate systems X_1-Y_1 and X_2-Y_2 . Using the assumption that the beam is thin, then the axial strain of this structure can be expressed as

$$\varepsilon_x = -z \frac{\partial^2 \omega_{rel,i}}{\partial x_i^2}, \quad i = 1,2 \quad (3.2)$$

where x_i is the scalar in the respective fixed coordinate system and the variable z represents the distance from the point of interest to the neutral axis and $\frac{\partial^2 \omega_{rel,i}}{\partial x_i^2}$ is the second derivative of the deformation in each beam section or approximately $1/R_i$, where R_i is the radius of curvature in a respective section.

The bending stress in the beam and the piezoelectric layer can be written as

$$\sigma_b = E_b \varepsilon_b \quad \text{and} \quad \sigma_p = E_p \varepsilon_p - e_{31} E_3, \quad (3.3)$$

where e_{31} is the coupling constant and E_3 is the electric field that is generated across the piezoelectric element in the three material direction. The z components can be written as

$$E_3 = -\frac{V(t)}{(h_2 + h_1 - Z_n)}. \quad (3.4)$$

The final equation is Ohm's law and states that the current (Q) flowing across a resistor (R) is proportional to the voltage ($V(t)$) across the resistor

$$V(t) = RQ. \quad (3.5)$$

The total displacement for the first beam can be written as

$$w_1 = w_{rel1}(x_1, t) + w_b(t). \quad (3.6)$$

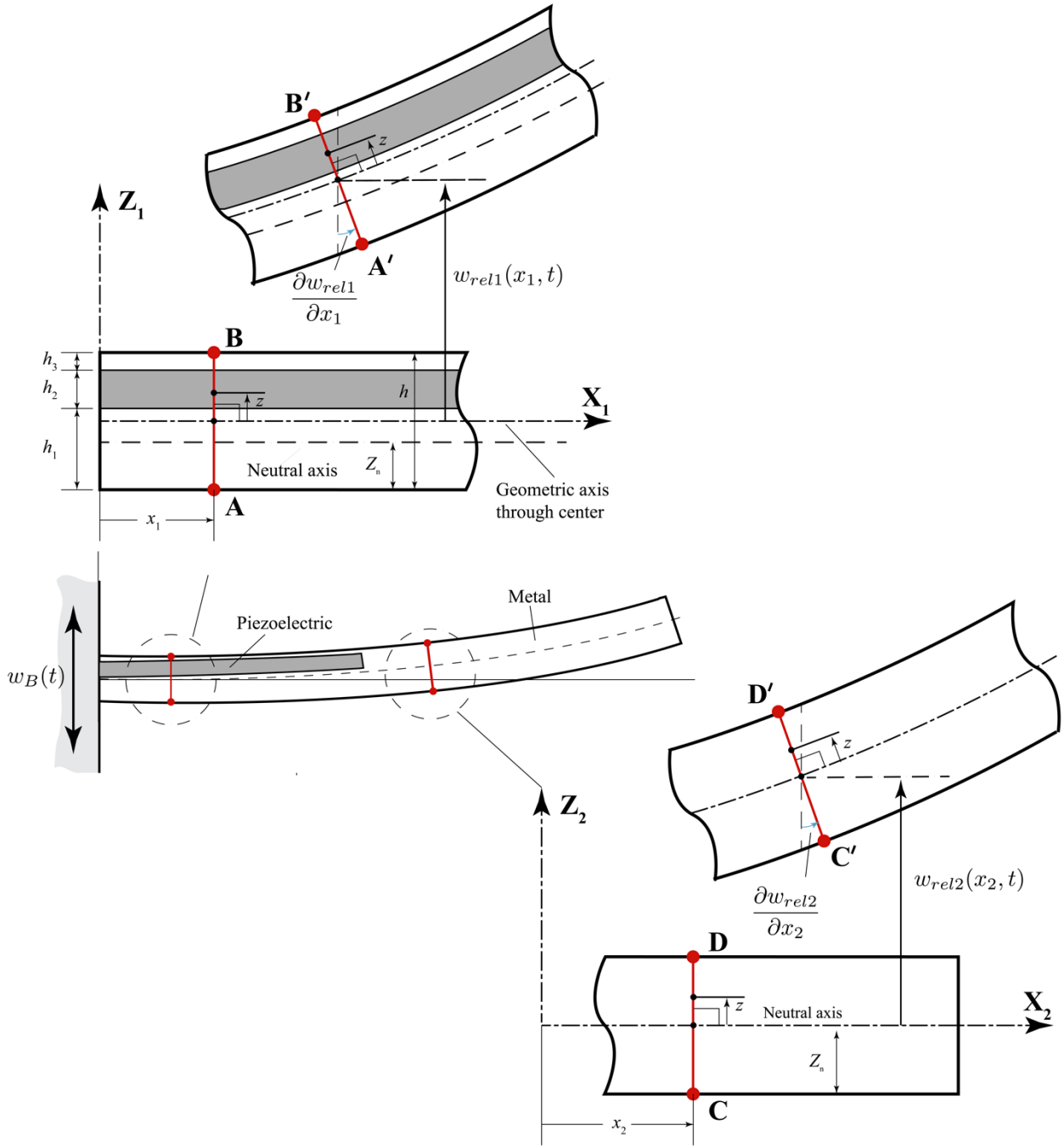


Figure 2: Displacement field for an Euler-Bernoulli beam with an embedded piezoelectric element, shown in gray.

where $w_{rel1}(x_1, t)$ denotes the transverse deflection of the first beam and $w_b(t)$ represents the transverse motion of the beam relative to the base. Furthermore, the displacement for the second beam can be written as

$$w_2 = w_{rel2}(x_2, t) + w_{rel1}(l, t) + x_2 \partial w_{rel1}(l, t) / \partial x_1. \quad (3.7)$$

The Hamilton's principle was used to obtain the coupled electromechanical behavior of the whole beam by integrating the Lagrangian over time

$$\int_{t_1}^{t_2} L dt = \int_{t_1}^{t_2} (T - U + W_E + W_{NC}) dt, \quad (3.8)$$

where the time t_2 and t_1 are arbitrary, T the kinetic energy, U the potential energy, W_E the electrical work and W_{NC} the work done by the nonconservative forces. In the sections that follow the Lagrangian will be split into two parts and variational calculus will be used to derive the governing equations, continuity equations, and boundary conditions.

3.1.1 Energy Expressions

Calculating the energy of the beam, one must account for the change in material in the cross section of the composite beam from metal to piezoelectric element and back to metal. The kinetic energy in the first beam can be written in the following form

$$\begin{aligned} T = & \frac{1}{2} \int_0^l \int_{-\frac{b}{2}}^{\frac{b}{2}} \int_{-z_n}^{h_1-z_n} \rho_b \left(\frac{\partial w_1}{\partial t} \right)^2 dz dy dx_1 \\ & + \frac{1}{2} \int_0^l \int_{-\frac{b}{2}}^{\frac{b}{2}} \int_{h_1-z_n}^{h_2+h_1-z_n} \rho_p \left(\frac{\partial w_1}{\partial t} \right)^2 dz dy dx_1 \\ & + \frac{1}{2} \int_0^l \int_{-\frac{b}{2}}^{\frac{b}{2}} \int_{h_2+h_1-z_n}^{h_3+h_2+h_1-z_n} \rho_b \left(\frac{\partial w_1}{\partial t} \right)^2 dz dy dx_1. \end{aligned} \quad (3.9)$$

Integrating Eqn. (3.9) allows the kinetic energy can be simplified as

$$T = \frac{1}{2} \int_0^l \rho A_{eff1} \left(\frac{\partial w_1}{\partial t} \right)^2 dx_1, \quad (3.10)$$

where ρA_{eff1} represents the beam mass per unit of length and is equal to $[\rho_b(h_1 + h_3) + \rho_p(h_2)]b$.

Similarly, the strain energy can be written as

$$\begin{aligned} U = & \frac{1}{2} \int_0^l \int_{-\frac{b}{2}}^{\frac{b}{2}} \int_{-z_n}^{h_1-z_n} \sigma_b \varepsilon_b dz dy dx_1 + \frac{1}{2} \int_0^l \int_{-\frac{b}{2}}^{\frac{b}{2}} \int_{h_1-z_n}^{h_2+h_1-z_n} \sigma_p \varepsilon_p dz dy dx_1 \\ & + \frac{1}{2} \int_0^l \int_{-\frac{b}{2}}^{\frac{b}{2}} \int_{h_2+h_1-z_n}^{h_3+h_2+h_1-z_n} \sigma_b \varepsilon_b dz dy dx_1 \end{aligned} \quad (3.11)$$

Integrating Eqn. (3.11), the potential energy can be simplified as

$$U = \frac{1}{2} \int_0^l EI_{eff1} \left(\frac{\partial^2 w_{rel1}(x_1, t)}{\partial x_1^2} \right)^2 dx_1 - \frac{1}{2} \int_0^l e_{31} H_p V(x_1, t) \left(\frac{\partial^2 w_{rel1}(x_1, t)}{\partial x_1^2} \right) dx_1. \quad (3.12)$$

The flexural rigidity EI_{eff1} and first moment of arear H_p are defined as

$$EI_{eff1} = \frac{E_b}{3} (h_1^3 + 3h_1^2 h_3 - 3h_1^2 Z_n + 6h_1 h_2 h_3 + 3h_1 h_3^2 - 6h_1 h_3 Z_n + 3h_1 Z_n^2 + 3h_2^2 h_3 + 3h_2 h_3^2 - 6h_2 h_3 Z_n + h_3^3 - h_3^2 Z_n + h_3 Z_n^2) b + \frac{E_p}{3} (3h_1^2 h_2 + 3h_1 h_2^2 - 6h_1 h_2 Z_n + h_2^3 - 3h_2^2 Z_n + 3h_2 Z_n^2) b, \quad (3.13)$$

and

$$H_p = \frac{b}{2} (2h_1 + h_2 - 2Z_n). \quad (3.14)$$

The electrical potential energy can be written as

$$W_E = \int_0^l \int_{-\frac{b}{2}}^{\frac{b}{2}} \int_{h_1 - Z_n}^{h_2 + h_1 - Z_n} E_3 D dz dy dx_1, \quad (3.15)$$

where the electrical displacement D is

$$D = e_{31} \varepsilon_p + \varepsilon_{33} E_3 \quad (3.16)$$

Plugging Eqn. (3.16) into Eqn. (3.15) the electrical potential can be simplified as

$$W_E = \frac{1}{2} \int_0^l e_{31} \frac{bh_2(2h_1 + h_2 - 2Y_n)}{2(h_2)} V(t) \left(\frac{\partial^2 w_{rel1}}{\partial x_1^2} \right) dx_1 + \frac{1}{2} \int_0^l \varepsilon_{33} \frac{h_2 b}{(h_2)^2} V^2(t). \quad (3.17)$$

The nonconservative work equation can be written as

$$W_{NC} = -VQ, \quad (3.18)$$

The variational equations should be obtained from the kinetic energy, the mechanical potential, the electrical potential, and the work done by nonconservative forces.

The variation of the kinetic energy of the first beam can be written as

$$\int_{t_1}^{t_2} \delta T dt = \int_{t_1}^{t_2} \left\{ \int_0^l \rho A_{eff1} \left(\frac{\partial^2 w_{rel1}(x_1, t)}{\partial t^2} \delta w_{rel1}(x_1, t) + \frac{\partial^2 w_b}{\partial t^2} \delta w_{rel1}(x_1, t) \right) dx_1 \right\} dt. \quad (3.19)$$

Using integration by parts the variation of the strain energy of the first beam can be written as:

$$\begin{aligned} \int_{t_1}^{t_2} \delta U dt = \int_{t_1}^{t_2} \left\{ \int_0^l E I_{eff1} \frac{\partial^4 w_{rel1}(x_1, t)}{\partial x_1^4} \delta w_{rel1}(x_1, t) dx_1 \right. \\ - \left[E I_{eff1} \frac{\partial^3 w_{rel1}(x_1, t)}{\partial x_1^3} \delta w_{rel1}(x_1, t) \right]_0^l \\ + \left[E I_{eff1} \frac{\partial^2 w_{rel1}(x_1, t)}{\partial x_1^2} \delta \left(\frac{\partial w_{rel1}(x_1, t)}{\partial x_1} \right) \right]_0^l \\ - \frac{1}{2} \int_0^l e_{31} H_{p1} \left(\frac{\partial^2 w_{rel1}(x_1, t)}{\partial x_1^2} \right) \delta V(t) dx_1 \\ \left. - \frac{1}{2} \left[e_{31} H_{p1} V(t) \delta \left(\frac{\partial w_{rel1}(x_1, t)}{\partial x_1} \right) \right]_0^l \right\} dt \end{aligned} \quad (3.20)$$

The electrical potential energy of the first beam can be written as

$$\begin{aligned} \int_{t_1}^{t_2} \delta W_e dt = \int_{t_1}^{t_2} \left\{ \frac{1}{2} \int_0^l e_{31} H_{p1} \left(\frac{\partial^2 w_{rel1}}{\partial x_1^2} \right) \delta V(t) dx_1 \right. \\ \left. + \frac{1}{2} \left[e_{31} H_{p1} V(t) \delta \left(\frac{\partial w_{rel1}}{\partial x_1} \right) \right]_0^l + \frac{1}{2} \int_0^l \epsilon_{33} \frac{b}{h_2} V^2(t) dx_1 \right\} dt \end{aligned} \quad (3.21)$$

Finally, the nonconservative work of the first beam can be written as

$$\int_{t_1}^{t_2} \delta W_{NC} dt = \int_{t_1}^{t_2} Q \delta V dt \quad (3.22)$$

Similar to the analysis for the first beam, the kinetic energy of the second beam can be expressed as

$$T = \frac{1}{2} \int_0^L \int_{-\frac{b}{2}}^{\frac{b}{2}} \int_{-\frac{h}{2}}^{\frac{h}{2}} \rho_b \left(\frac{\partial w}{\partial t} \right) \left(\frac{\partial w}{\partial t} \right) dz dy dx_2. \quad (3.23)$$

While the strain energy of the second beam can be written as

$$U = + \frac{1}{2} \int_1^L E_2 I_{eff2} \left(\frac{\partial^2 w_{rel2}(x_2, t)}{\partial x_2^2} \right)^2 dx_2 \quad (3.24)$$

where the constant $E_2 I_{eff2}$ is equal to $E_b (h^3/12) b$.

The variation in kinetic energy can be written as

$$\begin{aligned}
\int_{t_1}^{t_2} \delta T dt = & \int_0^L + \rho A_{eff2} \int_{t_1}^{t_2} \left\{ \left(-\frac{\partial^2 w_{rel2}(x_2, t)}{\partial t^2} - \frac{\partial^2 w_{rel1}(l, t)}{\partial t^2} - \frac{\partial^2 w_b(t)}{\partial t^2} \right. \right. \\
& \left. \left. - x_2 \frac{\partial^2 w_{rel1}'(l, t)}{\partial x_1^2} \right) \delta w_{rel2}(x_2, t) \right. \\
& + \left(-\frac{\partial^2 w_{rel1}(l, t)}{\partial t^2} - \frac{\partial^2 w_{rel2}(x_2, t)}{\partial t^2} - \frac{\partial^2 w_b(t)}{\partial t^2} \right. \\
& \left. \left. - x_2 \frac{\partial w_{rel1}'(l, t)}{\partial x_1} \right) \delta w_{rel1}(l, t) \right. \\
& + \left(-\frac{\partial^2 w_{rel2}(x_2, t)}{\partial t^2} - \frac{\partial^2 w_{rel1}(l, t)}{\partial t^2} - \frac{\partial^2 w_b(t)}{\partial t^2} \right. \\
& \left. \left. - x_2 \frac{\partial^2 w_1'(l, t)}{\partial x_1^2} \right) \delta w'_{rel1}(l, t) \right\} dt dx_2
\end{aligned} \tag{3.25}$$

The variation in strain energy can be written as

$$\begin{aligned}
\int_{t_1}^{t_2} \delta U dt = & \int_{t_1}^{t_2} \left\{ + \int_l^L E_2 I_{eff2} \frac{\partial^4 w_{rel2}(x_2, t)}{\partial x_2^4} \delta w_{rel2} dx_2 \right. \\
& \left. - \left[E_2 I_{eff2} \frac{\partial^3 w_{rel2}(x_2, t)}{\partial x_2^3} \delta w_{rel2}(x_2, t) \right]_l^L \right. \\
& \left. + \left[E_2 I_{eff2} \frac{\partial^2 w_{rel2}(x_2, t)}{\partial x_2^2} \delta \left(\frac{\partial w_{rel2}(x_2, t)}{\partial x_2} \right) \right]_l^L \right\} dt,
\end{aligned} \tag{3.26}$$

3.2 Governing Equations and Boundary Conditions

Grouping the similar variational terms under the integrand and at the boundaries yields the following equations of motion.

$$\rho A_{eff1} \frac{\partial^2 w_{rel1}}{\partial t^2} + EI_{eff1} \frac{\partial^4 w_{rel1}}{\partial x_1^4} = -\rho A_{eff1} A \omega_0^2 \sin(\omega_0 t), \quad (3.27)$$

$$\begin{aligned} \rho A_{eff2} \left(\frac{\partial^2 w_{rel2}}{\partial t^2} + \frac{\partial^2 w_{rel1}(l, t)}{\partial t^2} + \frac{\partial^2 w_b(t)}{\partial t^2} + x_2 \frac{\partial^3 w_{rel1}(l, t)}{\partial x_1 \partial t^2} \right) \\ + EI_{eff2} \frac{\partial^4 w_{rel2}}{\partial x_2^4} = 0, \end{aligned} \quad (3.28)$$

$$\int_0^l \theta \left(\frac{\partial^2 w_{rel1}}{\partial x^2} \right) + R \frac{dQ}{dt} + Q = 0. \quad (3.29)$$

Eqn. (3.27) and Eqn. (3.28) describes the mechanical governing equation, while the Eqn. (3.29) is the electrical governing equation, the electromechanical coupling is represented by θ and is equal to $e_{31} H_{p1}$, C_p is the capacitance of the piezoelectric element layer and is equal to $\varepsilon_{33} \frac{b}{h_2}$. The boundary conditions can be written as

$$w_{rel1}(0, t) = 0, \quad (3.30)$$

$$\frac{\partial w_{rel1}}{\partial x_1}(0, t) = 0, \quad (3.31)$$

$$w_{rel2}(0, t) = 0, \quad (3.32)$$

$$\frac{\partial w_{rel2}}{\partial x_2}(0, t) = 0, \quad (3.33)$$

$$EI_{eff2} \frac{\partial^3 w_{rel2}(L, t)}{\partial x_2^3} = 0, \quad (3.34)$$

$$EI_{eff2} \frac{\partial^2 w_{rel2}(L, t)}{\partial x_2^2} = 0. \quad (3.35)$$

and are obtained by grouping that variation at $x_1=0$ and $x_2=L$. The continuity between the two beams can be written as

$$\begin{aligned}
EI_{eff1} \frac{\partial^3 w_{rel1}(l, t)}{\partial x_1^3} &= \int_0^L \rho A_{eff2} \left(\frac{\partial^2 w_{rel1}(l, t)}{\partial t^2} + \frac{\partial^2 w_{rel2}(x_2, t)}{\partial t^2} + \frac{\partial^2 w_b(t)}{\partial t^2} \right. \\
&\quad \left. + x_2 \frac{\partial^3 w_{rel1}(l, t)}{\partial x_1 \partial t^2} \right) dx_2, \tag{3.36}
\end{aligned}$$

gives the continuity of shear and

$$\begin{aligned}
-EI_{eff1} \frac{\partial^2 w_{rel1}(x_1, t)}{\partial x_1^2} + \theta V(t) &= \int_0^L \rho A_{eff2} \left(\frac{\partial^2 w_{rel2}(x_2, t)}{\partial t^2} + \frac{\partial^2 w_{rel1}(l, t)}{\partial t^2} + \frac{\partial^2 w_b(t)}{\partial t^2} \right. \\
&\quad \left. + x_2 \frac{\partial^3 w_{rel1}(l, t)}{\partial x_1 \partial t^2} \right) x_2 dx_2. \tag{3.37}
\end{aligned}$$

gives the continuity of moments.

3.3 Free Vibration

In order to solve the free vibration problem base acceleration is set to zero and the composite beam is assumed to be operating under short circuit conditions, i.e., the resistive load approaches zeros. This yields the following equations

$$\rho A_{eff1}(x_1) \frac{\partial^2 w_{rel1}}{\partial t^2} + EI_{eff1}(x_1) \frac{\partial^4 w_{rel1}}{\partial x_1^4} = 0, \tag{3.38}$$

$$\rho A_{eff2} \left(\frac{\partial^2 w_{rel2}}{\partial t^2} + \frac{\partial^2 w_{rel1}(l, t)}{\partial t^2} + x_2 \frac{\partial^3 w_{rel1}(l, t)}{\partial x_1 \partial t^2} \right) + EI_{eff2} \frac{\partial^4 w_{rel2}}{\partial x_2^4} = 0. \tag{3.39}$$

along with comparable changes to the boundary conditions.

Next, the method of the separation of the variables was used to decompose the displacement of the two beams in a temporal (T_1 and T_2) and a spatial coordinate (W_1 and W_2) components in the form

$$w_{rel1}(x_1, t) = W_1(x_1)T_1(t), \text{ and } w_{rel2}(x_2, t) = W_2(x_2)T_2(t), \tag{3.40}$$

Substituting the definition of $w_{rel1}(x_1, t)$ in Eqn. (3.38) into Eqn.(.) leads to the following

$$\rho A_{eff1} W_1''''(x_1) T_1(t) + EI_{eff1} W_1(x_1) \ddot{T}_1(t) = 0, \quad (3.41)$$

where prime denotes the derivative with respect to the spatial coordination. Equation () can be rearranged as

$$\frac{EI_{eff1} W_1''''(x_1)}{\rho A_{eff1} W_1(x_1)} = \frac{\ddot{T}_1(t)}{T_1(t)} = -\omega^2, \quad (3.42)$$

solutions to $W_1(x_1)$ can be expressed as

$$W_1(x_1) = C_1 \sin \beta_1 x_1 + C_2 \cos \beta_1 x_1 + C_3 \sinh \beta_1 x_1 + C_4 \cosh \beta_1 x_1, \quad (3.43)$$

where $\beta_1^4 = \omega^2 \rho A_{eff1} / EI_{eff1}$.

Substituting into Eqn. () and noting that $T_2(t) = T_1(t)$ and can factored out of the governing equation to yield

$$EI_{eff2} W_2''''(x_2) T_1(t) - \rho A_{eff1} \omega^2 [W_2(x_2) + x_2 W_1'(L_1) + W_1(L_1)] = 0, \quad (3.44)$$

The solution to Eqn. () using the homogenous boundary conditions of the second beam

$$W_2(x_2) = D_1 \sin \beta_2 x_2 + D_2 \cos \beta_2 x_2 + D_3 \sinh \beta_2 x_2 + D_4 \cosh \beta_2 x_2 - x_2 W_1'(L_1) - W_1(L_1) \quad (3.45)$$

Using the homogenous boundary conditions of the second beam the solution can be simplified to

$$W_2(x_2) = D_1 \sin \beta_2 x_2 + D_2 (\cos \beta_2 x_2 - \cosh \beta_2 x_2) + D_3 \sinh \beta_2 x_2 - x_2 W_1'(L_1) + W_1(L_1) (1 - \cosh \beta_2 x_2), \quad (3.46)$$

where the values of the constants C_1, C_2, D_1, D_2, D_3 is determined by the remaining boundary conditions. The wave numbers β_1 and β_2 are related by

$$\frac{EI_{eff1}}{\rho A_{eff1}} \beta_1^4 = \frac{EI_{eff2}}{\rho A_{eff2}} \beta_2^4, \quad (3.47)$$

and corresponding to the same modal frequencies ω . The boundary conditions can be written as matrix equation whose entries are function of a single wavenumber, see Eqn. (). Here we, seek a nontrivial solution to this system of equations which can be determined by setting the determinant of the matrix to zero. The matrix entries A_{ij} are reported in Appendix B.

$$\begin{bmatrix} A_{11} & A_{12} & A_{13} & A_{14} & A_{15} \\ A_{21} & A_{22} & A_{23} & A_{24} & A_{25} \\ A_{31} & A_{32} & A_{33} & A_{34} & A_{35} \\ A_{41} & A_{42} & A_{43} & A_{44} & A_{45} \\ A_{51} & A_{52} & A_{53} & A_{54} & A_{55} \end{bmatrix} \begin{Bmatrix} C_1 \\ C_2 \\ D_1 \\ D_2 \\ D_3 \end{Bmatrix} = \begin{Bmatrix} 0 \\ 0 \\ 0 \\ 0 \\ 0 \end{Bmatrix} \quad (3.48)$$

The determinant of Eqn. (3.48) gives the characteristic equation of this structure. The characteristic equation is transcendental and must be solved numerically. In this case a script was written in MATLAB to determine the eigenvalues, $\beta_1 L$, and the corresponding modal frequencies.

This chapter has presented the formulation for the equation of motion of an Euler-Bernoulli beam with an embedded piezoelectric element. The analytical model was validated with FEA analysis using the commercial code PATRAN. In the next chapter, these results will provide the basis for a modal superposition representation of the response of the beam under a base excitation.

CHAPTER 4

DYNAMIC OF THE Al3003/PVDF/Al3003 STEPPED BEAM

In this chapter a study of the dynamic of the Al3003/PVDF/Al3003 is developed and then, the FEA model, used to prove the analytical results obtained, is described.

4.1 Orthogonality of Normal Modes Euler-Bernoulli Model with Embedded Element

An orthogonality of normal modes condition analysis was necessary in order to solve the Forced vibration problem and obtain the results needed. Since a stepped beam analysis was done, two orthogonality conditions were studied (the former for the first part of the beam and the latter for the second part of it), and then, to be coherent with the assumptions made, the solution of both cases were added to obtain the orthogonality condition valid for whole model.

4.1.1 First Part of the Beam

The orthogonality condition is derived using the boundary conditions (3.30) – (3.37) and (3.27), (3.28) that represent the mechanical governing equation of the motion of the first beam and the electrical governing equation that govern the PVDF sensor layer.

The eigenvalue problem can be solved considering an harmonic solution, with frequency ω :

$$\frac{d^2}{dx^2} [EI_{eff1} \frac{d^2 W_1(x_1)}{dx^2}] = \omega_1^2 \rho A_{eff1} W_1(x_1) \quad (4.1)$$

To derive the orthogonality equation the first section of the beam, two eigenvalues ω_{i1}^2 and ω_{j2}^2 and the relatives eigen functions $W_i(x_1)$, $W_j(x_1)$ were considered where i and j represents the modes while 1 and 2 represents the beam associated. So that:

$$\frac{d^2}{dx^2} \left[EI_{eff1} \frac{d^2 W_{i1}(x_1)}{dx^2} \right] = \omega_{i1}^2 \rho A_{eff1} W_{i1}(x_1) \quad (4.2)$$

And

$$\frac{d^2}{dx^2} \left[EI_{eff1} \frac{d^2 W_{j1}(x_1)}{dx^2} \right] = \omega_{j1}^2 \rho A_{eff1} W_{j1}(x_1) \quad (4.3)$$

Can be written.

Mathematically $\omega_{i1}^2, \omega_{i2}^2$ and $\omega_{j1}^2, \omega_{j2}^2$ have a different notation because one is referred to the first beam and the second one is referred to the second part of the structure, but, physically, the frequencies of the normal modes of these two beams are the same because it is the same structure but analyzed as two different structures. That allows the assumption that:

$$\omega_{i1}^2 = \omega_{i2}^2 \quad \& \quad \omega_{j1}^2 = \omega_{j2}^2 \quad (4.4)$$

Multiplying the (4.2) by $W_{j1}(x_1)$ and (4.3) by $W_{i1}(x_1)$, integrating by the length of the beam, plugging the boundary conditions and the continuity equations (3.30) – (3.37), and then subtracting the two equations resulting from these mathematical operations allows to write the orthogonality condition of the first beam as:

$$\begin{aligned} (\omega_{i1}^2 - \omega_{j1}^2) \int_0^l [\rho A_{eff1} W_{j1}(x_1) W_{i1}(x_1) \\ + \rho A_{eff2} (+W_{j1}(l)W_{i1}(l) + W_{j1}(l)W'_{i1}(l)x_2 \\ + W'_{j1}(l)W_{i1}(l)x_2 + W'_{j1}(l)W'_{i1}(l)x_2^2)] dx \\ + \omega_{i1}^2 \rho A_{eff2} \int_0^L [+W_{j1}(l)W_{i2}(x_2) + W'_{j1}(l)W_{i2}(x_2)x_2] dx_2 \\ - \omega_{j1}^2 \rho A_{eff2} \int_0^L [+W_{i1}(l)W_{j2}(x_2) + W'_{i1}(l)W_{j2}(x_2)x_2] dx_2 \\ = 0 \end{aligned} \quad (4.5)$$

4.1.2 Second Part of the Beam

Conforming to the analysis that was done for the first part of the beam, the orthogonality conditions is derived using the boundary conditions (3.30) – (3.37) and the equation (3.29) that represent the mechanical governing equation of the motion of the second part of the beam.

The eigenvalue problem can be solved considering an harmonic solution, with frequency ω :

$$\begin{aligned} E_2 I_{eff2} \frac{d^2}{dx^2} \left[E I_{eff2} \frac{d^2 W_2(x_2)}{dx^2} \right] \\ = \omega_1^2 \rho A_{eff2} [W_1(l) + W_2(x_2) \\ + x_2 W'_1(l)] \end{aligned} \quad (4.6)$$

To derive the orthogonality equation the second section of the beam, considering still valid the assumption made for (4.2) and (4.3). Two eigenvalues ω_{i1}^2 and ω_{j2}^2 and the relatives eigenfunctions $W_i(x_2)$, $W_j(x_2)$ were considered. So that:

$$\begin{aligned} E_2 I_{eff2} \frac{d^2}{dx^2} \left[E I_{eff2} \frac{d^2 W_{i2}(x_2)}{dx^2} \right] \\ = +\omega_{i1}^2 \rho A_{eff2} [W_{i1}(l) + W_{i2}(x_2) \\ + x_2 W'_{i1}(l)] \end{aligned} \quad (4.7)$$

And

$$\begin{aligned} E_2 I_{eff2} \frac{d^2}{dx^2} \left[E I_{eff2} \frac{d^2 W_{j2}(x_2)}{dx^2} \right] \\ = +\omega_{j1}^2 \rho A_{eff2} [W_{j1}(l) + W_{j2}(x_2) \\ + x_2 W'_{j1}(l)] \end{aligned} \quad (4.8)$$

Can be written

Multiplying the (4.7) equation by $W_{j2}(x_2)$ and (4.8) equation by $W_{i2}(x_2)$, integrating by the length of the beam, plugging the boundary conditions and the continuity equations (3.30) – (3.37), and then subtracting the two equations resulting from these mathematical operations allows to write the orthogonality condition of the first beam as:

$$\begin{aligned}
& (\omega_{i1}^2 - \omega_{j1}^2) \rho A_{eff2} \int_0^L W_{j2}(x_2) W_{i2}(x_2) dx + \omega_{i1}^2 \rho A_{eff2} \int_0^L [W_{j2}(x_2) W_{i1}(l) \\
& + W_{j2}(x_2) W'_{i1}(l) x_2] dx - \omega_{j1}^2 \rho A_{eff2} \int_0^L [W_{i2}(x_2) W_{j1}(l) \\
& + W_{i2}(x_2) W'_{j1}(l) x_2] dx
\end{aligned} \tag{4.9}$$

4.1.3 Orthogonality of Normal Modes Solution

Adding equation (4.5) with equation (4.9) and rearranging, will bring directly to the formulation searched :

$$\begin{aligned}
& (\omega_{i1}^2 - \omega_{j1}^2) \int_0^l [\rho A_{eff1} W_{j1}(x_1) W_{i1}(x_1) \\
& + \rho A_{eff2} (W_{j2}(x_2) W_{i2}(x_2) + W_{j1}(l) W_{i1}(l) + W_{j1}(l) W'_{i1}(l) x_2 \\
& + W'_{j1}(l) W_{i1}(l) x_2 + W'_{j1}(l) W'_{i1}(l) x_2^2 + W_{j1}(l) W_{i2}(x_2) \\
& + W'_{j1}(l) W_{i2}(x_2) x_2 + W_{j2}(x_2) W_{i1}(l) + W_{j2}(x_2) W'_{i1}(l) x_2)] dx = \delta_{ij}
\end{aligned} \tag{4.10}$$

(5.10) is called orthogonality of the normal modes, where δ_{ij} is the Kronecker delta defined as:

$$\delta_{ij} = \begin{cases} 0, & i \neq j \\ 1, & i = j \end{cases} \tag{4.11}$$

4.2.1 Forced Vibration Problem

In this section, the problem of the forced vibration of a stepped beam is investigated.

The first and the second subchapters contain the analysis of the forced vibration of the first and the second part of the beam, respectively, while the last subchapter contains the equation that governs the whole structure. As was done before, the forced vibration equation of the first and the second beam were added in order to obtain the equation that governs the structure. Then a passage from the modal coordinates to the physical one was done to obtain the real displacement that this beam has under a base excitation.

4.2.1.1 First Part of the Beam

Through the modal analysis approach, the solution of equation (3.27) can be written as a linear combination of the beam's normal modes such as:

$$w_{rel1}(x_1, t) = \sum_{i=1}^N W_{i1}(x_1) H_R e^{i\Omega t} \quad (4.12)$$

Where $w_{rel1}(x_1, t)$ is the displacement relatives to the first part of the beam, $W_{i1}(x_1)$ represents the normal mode found by solving the free vibration problem, H_R depicts the modal coordinates.

Plugging (4.12) into (3.27) -(3.28) and then factoring out $e^{i\Omega t}$, brings to the formulation of the governing equations of the first part of the beam for this kind of analysis:

$$\begin{cases} 1) - \rho A_{eff1} \Omega^2 W_{i1}(x) H_R + E I_{eff1} \frac{\partial^4 W_{i1}}{\partial x^4} H_R = + \rho A_{eff1} \Omega^2 W_b \\ 2) \int_0^l \theta i \Omega \left(\frac{\partial^2 W_{i1}(x)}{\partial x^2} \right) H_R dx + C_p i \Omega V_0 + \frac{V_0}{R} = 0 \end{cases} \quad (4.13)$$

Then multiply the first equation of (4.13) by $W_{j1}(x_1)$ and integrating over the length of the first beam, plugging (4.12) into the boundary conditions and the continuity equations (3.30) – (3.37) and rearranging, brings to the equation that rules the first part of the beam:

$$\begin{aligned}
& EI_{eff1} - \Omega^2 H_R \left[\rho A_{eff1} \int_0^l W_{i1}(x) W_{j1}(x) dx \right. \\
& + \rho A_{eff2} \int_0^L [W_{j1}(l) W_{i1}(l) + W_{j1}(l) W_{i2}(x_2) \\
& + W_{j1}(l) W'_{i1}(l) x_2] dx_2 \\
& + \rho A_{eff2} \int_0^L [W'_{j1}(l) W_{i1}(l) x_2 + W'_{j1}(l) W_{i2}(x_2) x_2 \\
& + W'_{j1}(l) W'_{i1}(l) x_2^2] dx_2 \left. \right] - \frac{\partial W_{j1}(l)}{\partial x} \theta V_0 \\
& + EI_{eff1} H_R \int_0^l \frac{\partial^2 W_{i1}(x)}{\partial x^2} \frac{\partial^2 W_{j1}(x)}{\partial x^2} dx \\
& = \Omega^2 W_b \left[\rho A_{eff1} \int_0^l W_{j1}(x) dx + \rho A_{eff2} \int_0^L W_{j1}(l) dx_2 \right. \\
& \left. + \rho A_{eff2} \int_0^L \frac{\partial W_{j1}(l)}{\partial x} x_2 dx_2 \right]
\end{aligned} \tag{4.14}$$

4.2.2 Second Part of the Beam

As was done for the first part of the beam, the governing equation of the motion is given by (3.27) – (3.29). Through the modal analysis approach, the solution of equation (3.29) can be written as a linear combination of the beam's normal modes such as:

$$w_{rel2} = \sum_{i=1}^N W_{i2}(x_2) H_R e^{i\Omega t} \tag{4.15}$$

Where $w_{rel2}(x_2, t)$ is the displacement relatives to the second part of the beam, $W_{i2}(x_2)$ represents the normal mode found by solving the free vibration problem, H_R depicts the modal coordinates.

Plugging (4.15) into (3.29), and Factoring out $e^{i\Omega t}$, it brings to the formulation of the forced vibration governing equations for the second part of the beam:

$$\begin{aligned}
& -\rho A_{eff2} (\Omega^2 H_R W_{i1}(l) + \Omega^2 H_R W_{i2}(x_2) + \Omega^2 W_b + x_2 \Omega^2 e^{i\Omega t} H_R \frac{\partial W_{i1}(l)}{\partial x_1}) \\
& + EI_{eff2} H_R \frac{\partial^4 W_{i2}(x_2)}{\partial x_2^4} = 0
\end{aligned} \tag{4.16}$$

Then, multiply (4.16) by $W_{j_2}(x_2)$ and integrating over the length of the second beam, plugging the result of the previous passage into the boundary conditions and the continuity equations (3.30) – (3.37) and rearranging. It brings to the equation that rules the second part of the beam:

$$\begin{aligned}
& \Omega^2 H_R \left[\rho A_{eff2} \int_0^L W_{j_2}(x) W_{i_2}(x_2) + W_{j_2}(x) W_{i_1}(l) + W_{j_2}(x) W'_{i_1}(l) x_2 dx \right] \\
& + EI_{eff2} H_R \left[\int_0^L \frac{\partial^2 W_{i_2}(x)}{\partial x^2} \frac{\partial^2 W_{j_2}(x)}{\partial x^2} dx \right] \\
& = \rho A_{eff2} \Omega^2 W_b \int_0^L W_{j_2}(x) dx
\end{aligned} \tag{4.17}$$

4.2.3 Forced Vibration Solution

The equation that rules the forced vibration problem of this beam can be found adding (4.14) and equation (4.17). This passage allows to write the solution equation that governs the forced vibration problem as:

$$\begin{aligned}
& \Omega^2 H_R \left[\rho A_{eff1} \int_0^l W_{i_1}(x_1) W_{j_1}(x_1) dx \right. \\
& + \rho A_{eff2} \int_0^L [W_{j_1}(l) W_{i_1}(l) + W_{j_1}(l) W_{i_2}(x_2) \\
& + W_{j_1}(l) W'_{i_1}(l) x_2 + W'_{j_1}(l) W_{i_1}(l) x_2 + W'_{j_1}(l) W_{i_2}(x_2) x_2 \\
& + W'_{j_1}(l) W'_{i_1}(l) x_2^2 + W_{j_2}(x_2) W_{i_2}(x_2) + W_{j_2}(x_2) W_{i_1}(l) \\
& \left. + W_{j_2}(x_2) W'_{i_1}(l) x_2] dx_2 \right] - \frac{\partial W_{j_1}(l)}{\partial x} \theta V_0 \\
& + EI_{eff1} H_R \int_0^l \frac{\partial^2 W_{i_1}(x_1)}{\partial x^2} \frac{\partial^2 W_{j_1}(x_1)}{\partial x^2} dx \\
& + EI_{eff2} H_R \left[\int_0^L \frac{\partial^2 W_{i_2}(x_2)}{\partial x^2} \frac{\partial^2 W_{j_2}(x_2)}{\partial x^2} dx \right] \\
& = \Omega^2 W_b \left[\rho A_{eff1} \int_0^l W_{j_1}(x_1) dx \right. \\
& \left. + \rho A_{eff2} \int_0^L \left[W_{j_1}(l) + W_{j_2}(x_2) + \frac{\partial W_{j_1}(l)}{\partial x} x_2 \right] dx_2 \right]
\end{aligned} \tag{4.18}$$

Noticing that, the first part of (4.18) is equal to the orthogonality condition (4.10) and assuming that $i=j$, so the Kroekner delta is equal to 1, neglectic the dumping effect, is possible to write equation (4.18) and the second equation of (4.13) as:

$$H_R(\omega_R^2 - \Omega^2) + 2i\xi\omega_r\Omega H_r - \chi_R V_0 = F_R \quad (4.19)$$

$$\sum_{r=1}^N i\Omega \chi_R H_R + i\Omega C_p V + \frac{V}{R} = 0 \quad (4.20)$$

Where the voltage V_0 is equal to:

$$V_0 = - \frac{\sum_{r=1}^N \frac{i\Omega \chi_R F_R}{(\omega_R^2 - \Omega^2 + 2i\xi\omega_r\Omega)}}{\left(\frac{1}{R} + i\Omega C_p + \sum_{r=1}^N \frac{i\Omega \chi_R^2}{(\omega_R^2 - \Omega^2 + 2i\xi\omega_r\Omega)}\right)} \quad (4.21)$$

The modal coordinate H_R is equal to:

$$H_R = \frac{1}{(\omega_R^2 - \Omega^2 + 2i\xi\omega_r\Omega)} \left(F_R - \chi_R \frac{\sum_{r=1}^N \frac{i\Omega \chi_R F_R}{(\omega_R^2 - \Omega^2 + 2i\xi\omega_r\Omega)}}{\left(\frac{1}{R} + i\Omega C_p + \sum_{r=1}^N \frac{i\Omega \chi_R^2}{(\omega_R^2 - \Omega^2 + 2i\xi\omega_r\Omega)}\right)} \right) \quad (4.22)$$

And the modal forcing F_R is :

$$F_R = \Omega^2 W_b \left\{ \rho A_{eff1} \int_0^L W_{j1}(x_1) dx + \rho A_{eff2} \int_0^L \left[W_{j1}(l) + W_{j2}(x_2) + \frac{\partial W_{j1}(l)}{\partial x} x_2 \right] dx_2 \right\} \quad (4.23)$$

4.3 FEA Model Description

In order to validate the analytical work done in this dissertation, a FEA model, with the PATRAN software, was done.

In Figure 3 is shown the model that was created for this purpose while the material geometries and the material properties are shown in the table ...

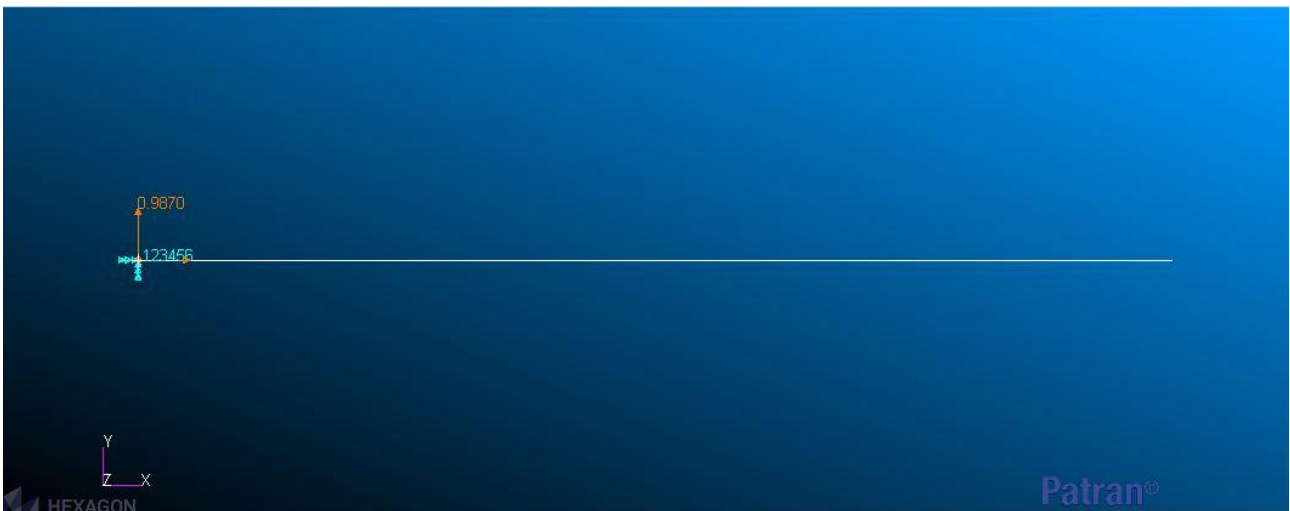


Figure 3: PATRAN model of the cantilever stepped beam with an embedded sensor used for the validation, lateral view.

The whole structure was created as the summation of two beams (to be coherent with the analytical analysis done in this work). The material's properties and geometries showed in Table 5.1 were added to the software, and then a composite material was created to reproduce the first part of the beam. Multiple ways to develop the material could be followed, one of them could be creating three 3D solid models with different material properties each other, put them one above the other and then, with the program, impose the contact between them. By the way, a composite model was preferred to have a lighter model and a faster NASTRAN software analysis.

After that, the properties were assigned. The composite material Al3003/PVDF/Al3003 with an orientation of 0 degrees was assigned to the first beam and the Al3003 to the second beam both as a 2D shell.

After these operations, the model was meshed with a mesh seed and then an Isomesh. A fixed static constraint was then associated with the nodes related to the first part of the beam's extremity because of the cantilever beam's assumption.

An observation should be done. Due to the student version that was used for this model, the mesh wasn't extremely tight. The PATRAN student edition limitation imposes a 5000 elements model, at least, but the mesh was tight enough to match the results from the MATLAB results for the whole analysis so a valid model was obtained.

Table 1: Material Properties and geometries of the analyzed beam

Property	PVDF	Al3003 (First Part of the Beam)	Al 3003 (Second Part of the Beam)
Young modulus	3000 MPa	75 GPa	75 GPa
Length	0.15 m	0.15 m	0.15 m
Width	0.01 m	0.01 m	0.01 m
Density	0.0001 m	1604.3	0.51%
Thickness	0.0001 m	0.0039 m	0.005 m
Piezoelectric Strain	1700 kg/m ³	2730 kg/m ³	2730 kg/m ³
Constant Relative Dielectric Constant	30 pC/N	NA	NA
	12	NA	NA

After this procedure, the model was ready for a normal modes analysis to obtain the normal modes' frequency and validate the free vibration solution, but it wasn't enough to satisfy the requirement of the FRF analysis in order to validate the forced vibration problem, so, a non-spatial frequency field with the required interval of frequencies and value of 0.987 G was created. This non-spatial field was then associated with the fixed constraint and the acceleration in the y-axis direction, and which became from static to time-dependent and the dumping value of 0.006 was added to the software.

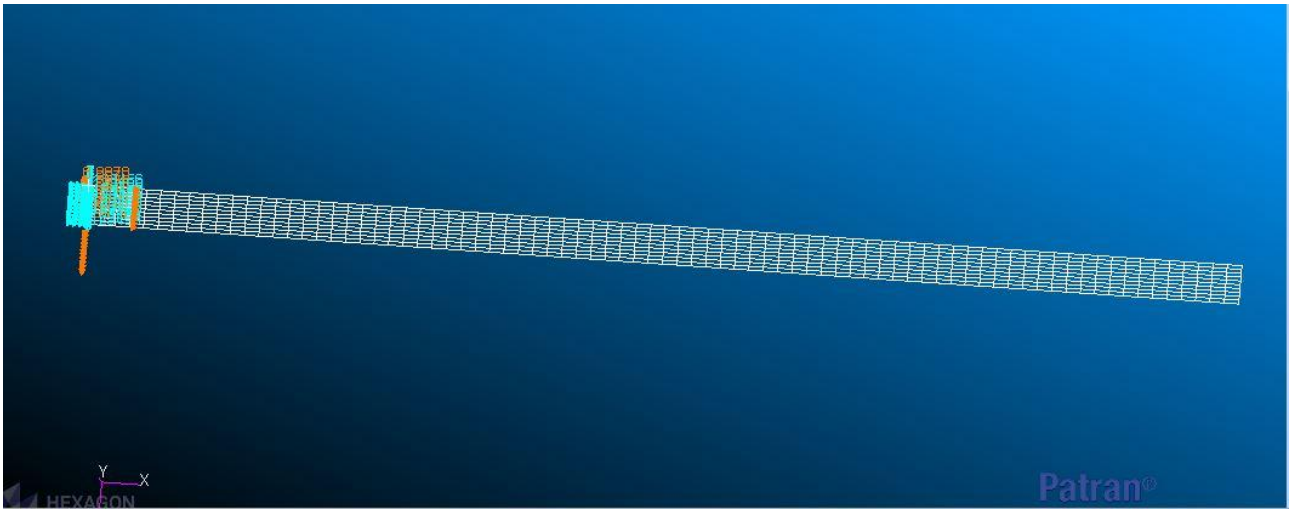


Figure 4: PATRAN model of the meshed cantilever stepped beam with an embedded sensor used for the validation, with base acceleration and constraints applied on the root.

4.3.1 FEA Model Validation

To validate the model described in section 4.3, a first analysis of the normal modes of a cantilever stepped beam made only in Al3003 was done. In order to use the same model described in the previous chapter, the PVDF layer was considered equal to zero and it was replaced with a layer of Al3003 with the same geometric properties.

Table 2 shows the results of the pre validation analysis and it can be stated that the frequency of the normal modes are coherent with the results obtained from the analytical model (it was used the model described in the third chapter with some modification). The analytical model shows higher results as the n th frequency of normal modes increase but the error is below 1%. In addition, the shapes of the normal modes obtained from the PATRAN software match with the shapes that was obtained from the analytical work done in chapter 3 so the FEA model model can be considerate accurate, reliable and used to compare the results of the analysis made with the PVDF sensor embedded.

Table 2: Comparison of modal frequency of the analytical solution and the FEA model for an Al3003 stepped beam

Mode	Analytical Result [Hz]	Finite Element Analysis [Hz]	% Error
1	47.0	47.0	0.01%
2	294.8	294.4	0.13%
3	825.4	823.1	0.27%
4	1617.5	1609	0.51%
5	2673.8	2651	0.82%

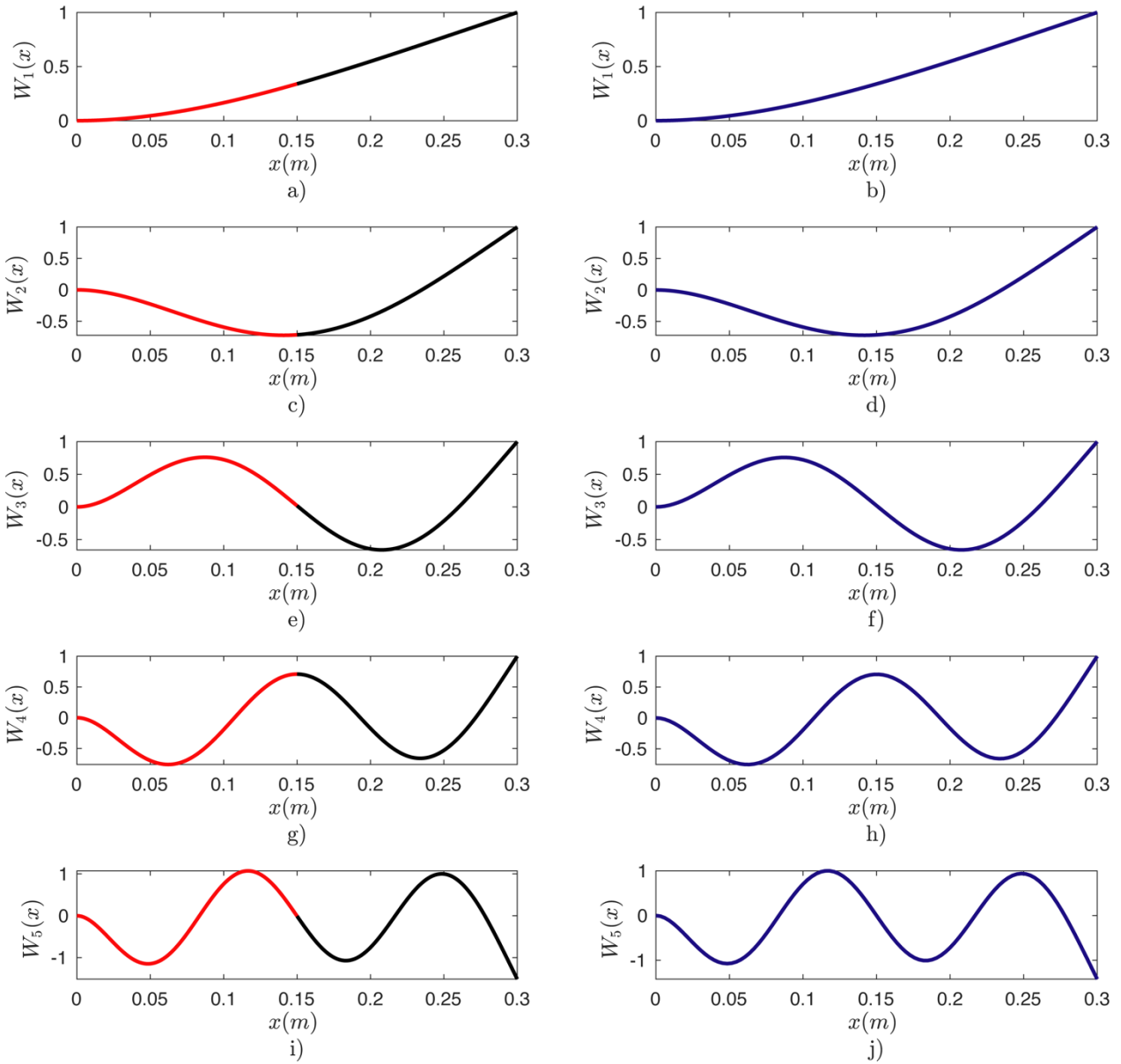


Figure 5: Modal shapes of Al3003 stepped beam: a), c), e), g), i) are analytical mode shapes, and b), d), f), h) and j) are the FEA mode shapes. The red line indicates beam section one and the black line indicates beam section two.

After the pre-validation, a validation of the normal modes and the displacement with the effective model (Al3003/PVDF/Al3003) was done. The results obtained from the analytical analysis are shown in the Table () and match accurately with the one obtained with the model presented in this dissertation, note that the models agree closely with the greatest percentage difference is less than 0.82%. Note that greatest error occurs at mode, the fundamental mode of the analytical mode and the FEA model differs by 0.01%. Figure 5 depicts both the analytical and finite element mode shapes. The modes are normalized by setting $W_2(L) = 1$. As expected the modes resemble those

of a cantilevered beam. Figure 1 a), c), e), g), i) are analytical mode shapes. The red line indicates beam section one and the black line indicates beam section two. Figure 2 b), d), f), h) and j) are the FEA mode shapes. Visually the modal shapes from the two analysis are indistinguishable.

The displacement is shown in the Table 2 and also matches with the one obtained from the PATRAN model with an error of 3.85%.

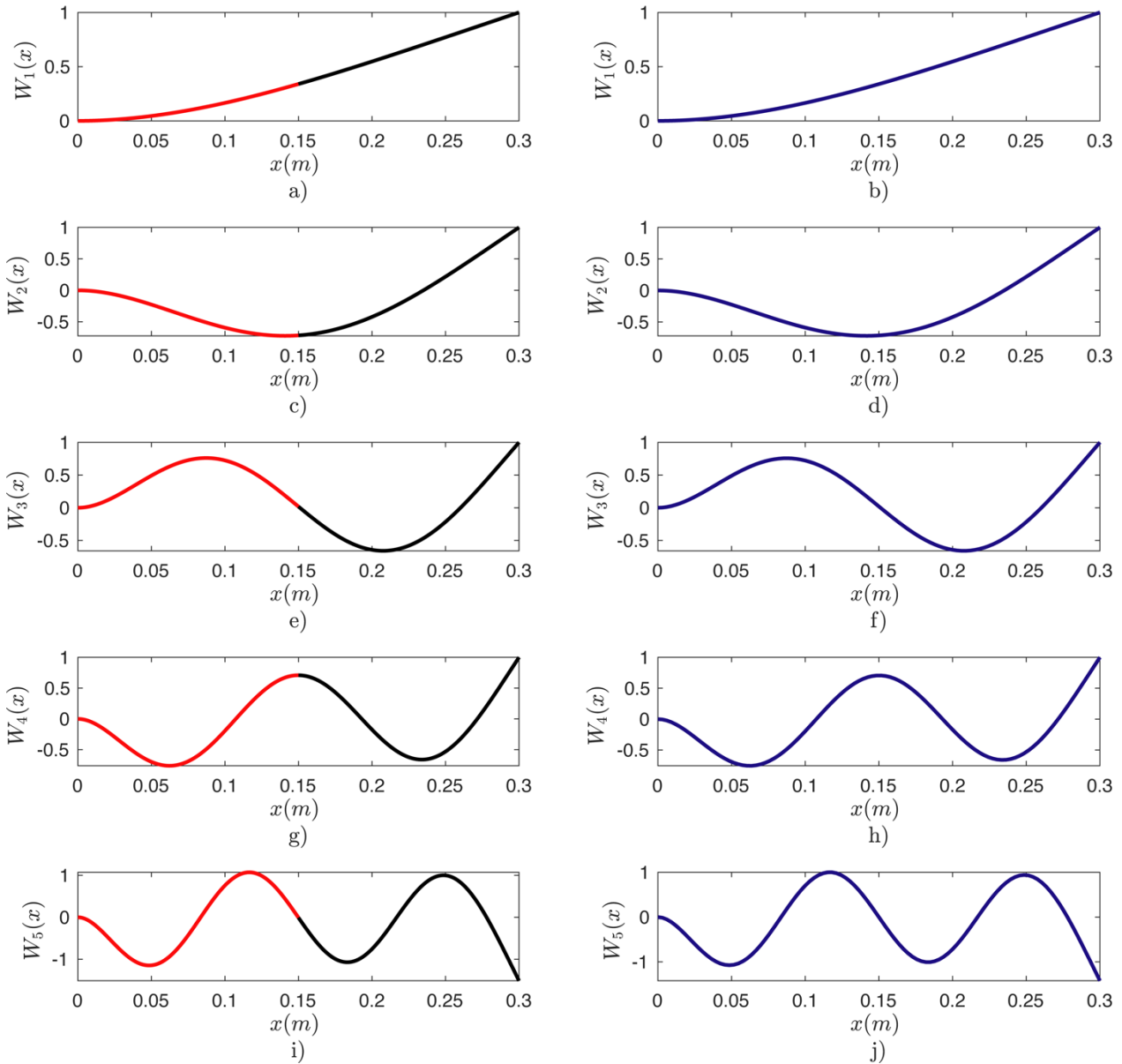


Figure 6: Modal shapes of of composite beam: a), c), e), g), i) are analytical mode shapes, and b), d), f), h) and j) are the FEA mode shapes. The red line indicates beam section one and the black line indicates beam section two.

Table 3: Comparison of modal frequencies of the analytical solution and FEA model.

Mode	Analytical [Hz]	Finite Element Analysis [Hz]	% Error
1	46.6	46.6	0.01%
2	293.6	293.3	0.13%
3	823	820.7	0.27%
4	1612.4	1604.3	0.51%
5	2665.6	2647.8	0.82%

Table 4: Displacement result comparison of the analytical solution and the FEA model, composite cantilever Al3003/PVDF/Al3003 beam

	Analytical [Hz]	Finite Element Analysis [Hz]	% Error
Displacement [m]	$2.5 * 10^{-3}$	$2.6 * 10^{-3}$	3.85%

CHAPTER 5

ANALYTICAL RESULTS

In order to understand the behavior and the response of the cantilever beam and the harvested voltage output under a base excitation, a parametric study with the model depicts in this dissertation was done. modifying four different variables is it possible to find the optimum geometry and resistance configuration:

1. PVDF layer length
2. PVDF layer position
3. PVDF layer thickness
4. Young modulus variation

The dimensions of the beam considerate d for this analysis are shown in table 1

5.1 PVDF Length Variation

In order to find the optimum length of the PVDF that allows a maximum of the voltage, a 3D parametric analysis was run. The parameters that were considered as variables were:

1. Length of the first part of the beam
2. The resistance of the equivalent circuit
3. Voltage output of the piezoelectric material

As regards the length variation it was considered an alpha parameter. The length of the first part of the beam (the one with the PVDF layer) was equal to alpha, while the length of the second one was $0.32 [m] - \alpha$, then, the Alpha variable was increased from 0 to L (the total length of the whole beam to obtain all the possible response of the structure. The range of the resistance was from 0 [Ohm] to 10^{11} [Ohm], higher values where not considered because these are non-physically possible for real application of this structure.

It is important to notice that the analysis presented in this dissertation was done under the Euler-Bernoulli theory, so, this results is accurate for alpha that respect the length restriction of the thin beam. When the first part of the beam or the second one is too short, the analysis doesn't show an accurate solution because it breaks the assumptions made.

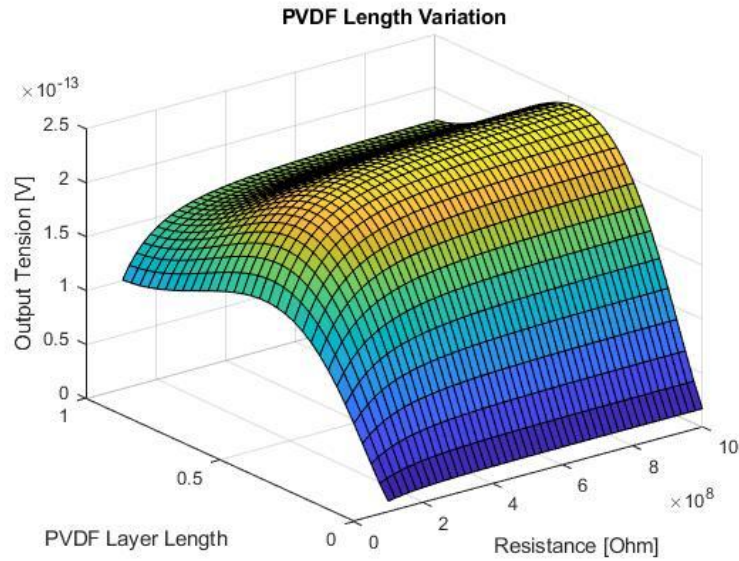


Figure 7: PVDF length 3D analysis variation. **X-axis**= resistance variation, **Y-axis**=piezoelectric layer's length, **Z-axis**= piezoelectric voltage output

Fig. 7 shows the results obtained from the analytical analysis. It is obvious that the maximum voltage output is reached when the first part of the beam's length is equal to the second part. In addition, the resistance behavior was as expected, a fast increase until the resistance is equal to $8e8$ and then the output value starts to increase slightly. As regards the Frequency of the first normal modes is possible to notice, from Fig 8 a minimum value when the length of the first part of the beam is equal to the second one so, when the output voltage of the piezoelectric material shows a maximum.

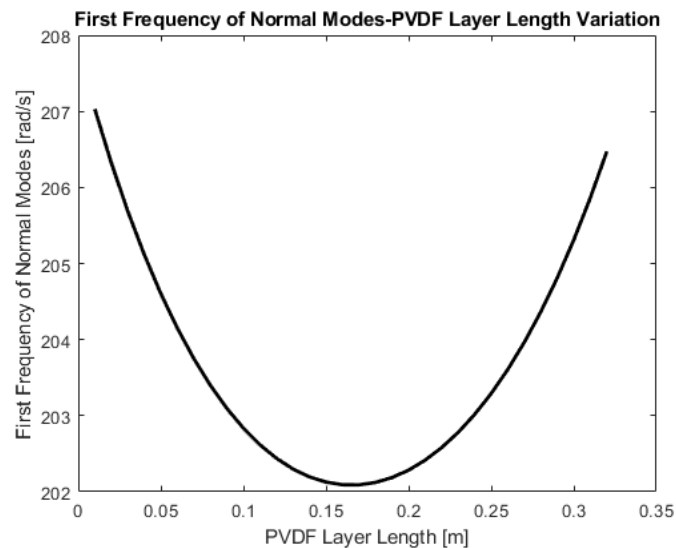


Figure 8: PVDF length-frequency of normal modes variation, 2D analysis, first frequency of normal modes variation with a fixed resistance of $8e8$ [Ohm], **X-axis**= length of the first part of the beam **Y-axis**=first frequency of normal modes.

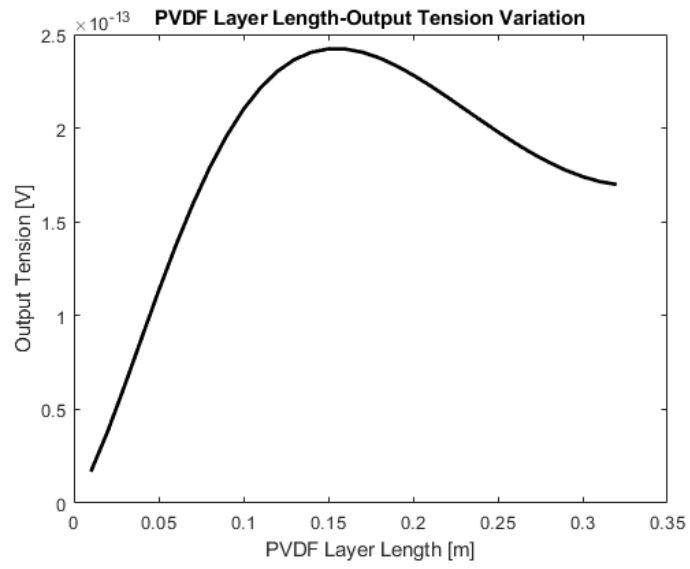


Figure 9: PVDF length-voltage output variation with fixed resistance of $8e8$ detail, 2D analysis, **X-axis:** α , **Y-axis:** piezoelectric material output tension

5.2 PVDF Layer Position

In order to find the optimum position of the PVDF that allows a maximum of the voltage, parametric analysis was run with three variables:

1. Position of the PVDF layer
2. The resistance of the equivalent circuit
3. Voltage output of the piezoelectric material

For this analysis, was considered a PVDF layer of $1/8$ of the thickness of the beam and a total thickness of 0.004m . The PVDF layer was moved from the top of the beam to the middle of it with an increase of $1/20$ of the total beam thickness. The piezoelectric material was moved until the middle of the beam because of the symmetrical geometry of the structure and then the symmetrical results.

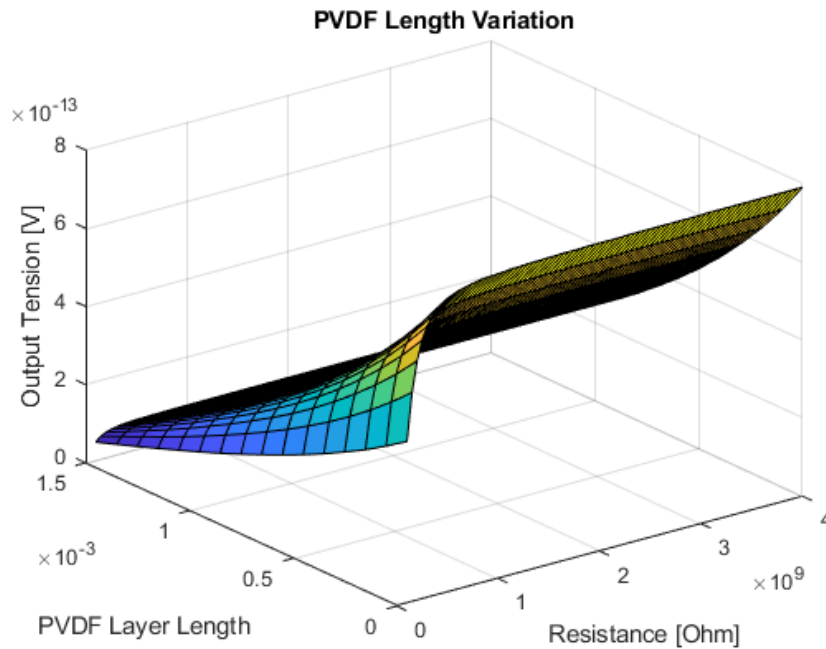


Figure 10: Piezoelectric layer Position variation, 3D analysis, **X-axis**= resistance variation, **Y-axis**=piezoelectric layer's length, **Z-axis**= piezoelectric voltage output

As shown in Fig. 10, the optimum of the voltage is found when the PVDF layer is placed on the top or on the bottom of the beam, where the strain developed is maximum. As regards the output variation between the **Y-Z** axis, as shown in Fig 13, it is possible to notice that the voltage output doesn't show a linear variation with the variation of the position but the curve is slightly flexed.

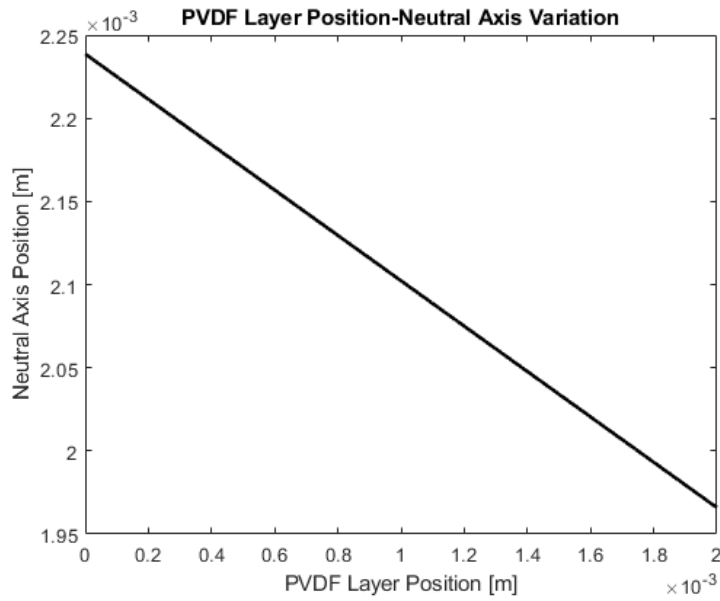


Figure 11: PVDF layer position-neutral axis variation, 2D analysis, **X-axis**= PVDF layer position, **Y-axis**=neutral axis position.

The analysis of the variation of the first frequency of the normal modes and the output tension of the piezoelectric material obtained shows, as expected, a symmetry in the results. The shapes of the curve shows a minimum when there the voltage output is maximum, at the top or at the bottom of the beam.

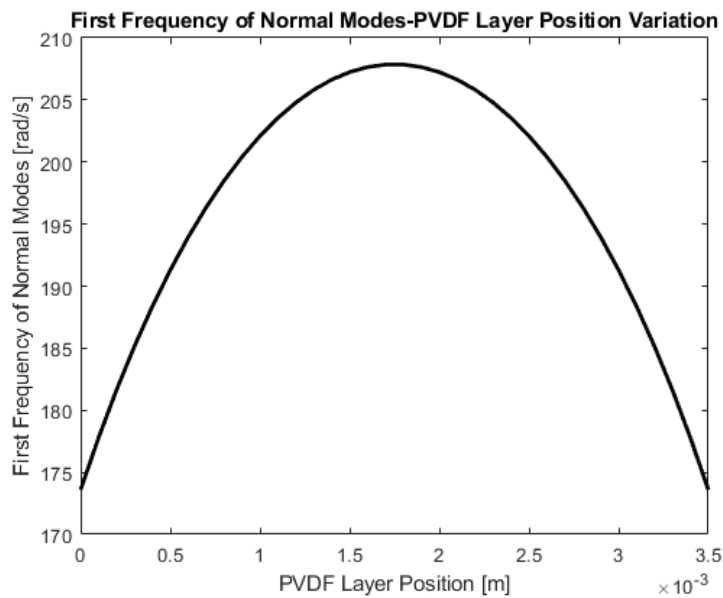


Figure 12: PVDF position-frequency of normal modes variation, 2D analysis, first frequency of normal modes variation with a fixed resistance of $8e8$ [Ohm], **X-axis**= PVDF position [m], **Y-axis**=first frequency of normal modes.

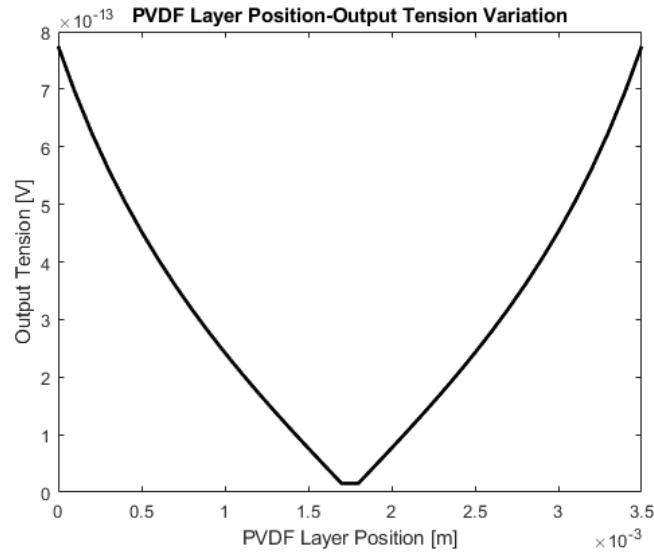


Figure 13: PVDF position-voltage output variation with fixed resistance of $8e8$ [Ohm] detail, 2D analysis, **X-axis**: PVDF layer position, **Y-axis**: piezoelectric material output tension

6.3 PVDF Layer Thickness

In order to find the optimum thickness of the PVDF that allows a maximum of the voltage harvesting, a parametric analysis was run. The parameters that were considered as variables were:

1. The thickness of the PVDF layer
2. The resistance of the equivalent circuit
3. Voltage output the piezoelectric material

The parametric analysis started with a PVDF layer a thickness equal of zero, it increased of $1/25$ of the total thickness of the beam and ended with a PVDF thickness equal to the thickness of the whole structure.

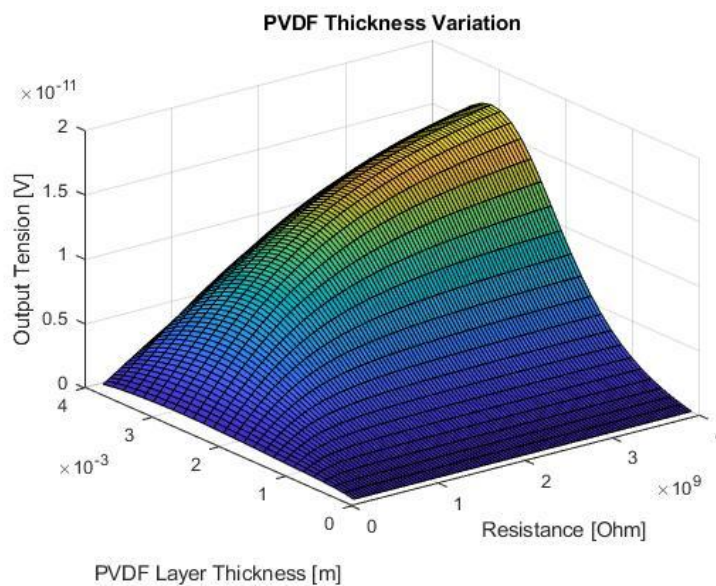


Figure 14: PVDF thickness variation, 3D analysis, **X-axis**= resistance variation, **Y-axis**= piezoelectric layer's thickness, **Z-axis**= piezoelectric voltage output

Fig 14 depicts the output voltage related to the variation of the resistance and the thickness of the PVDF structure. As is shown, the optimum of the voltage is not when the first part of the beam is made with only PVDF but when there is a part of base material and a part of PVDF. Fig. shows the variation of the Neutral axis related to the thickness of the PVDF material

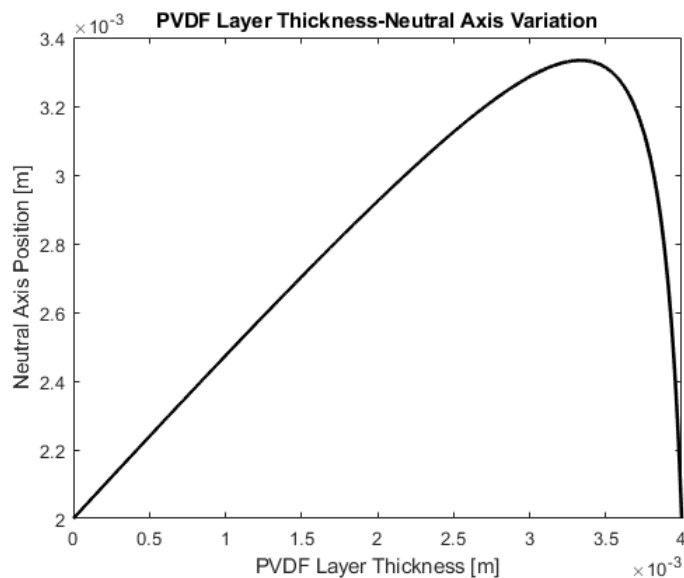


Figure 15: PVDF layer thickness-neutral axis variation, 2D analysis, **X-axis**= PVDF layer thickness, **Y-axis**= neutral axis position.

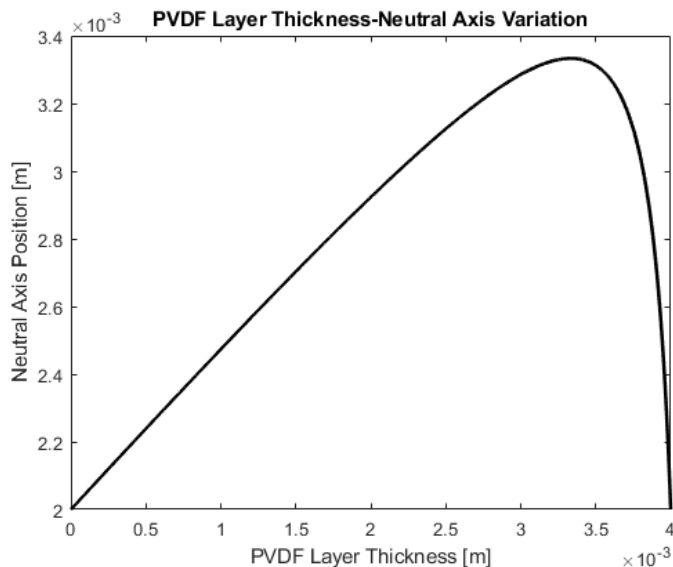


Figure 16: PVDF layer thickness-voltage output variation with fixed resistance of $8e8$ detail, 2D analysis, **X-axis**: PVDF layer thickness, **Y-axis**: piezoelectric material output tension

As the 3D analysis showed, is possible to understand that the maximum output voltage is found when the thickness of first part of the beam is equal to the 0.65% of the total thickness of the beam

5.4 YOUNG Modulus Variation

To relate the Young modulus of the base material with the Young modulus of the PVDF it was considered that the young modulus of the base material was equal to the Young modulus of the PVDF material multiplied by a variable that allows to obtain multiple materials based on his value, alpha. A 3D parametric analysis was run to understand the voltage output of the PVDF layer and the parameters considered as variables were:

1. Material Young modulus
2. Resistance of the equivalent circuit
3. Voltage output of the piezoelectric material

Fig. 17 depicts the solution of the analysis .It is possible to notice that the higher output voltage is obtained when the base material is softer and, the output tension decrease fast between alpha parameters from 0-7 Fig, then the voltage output decrease too but slower.

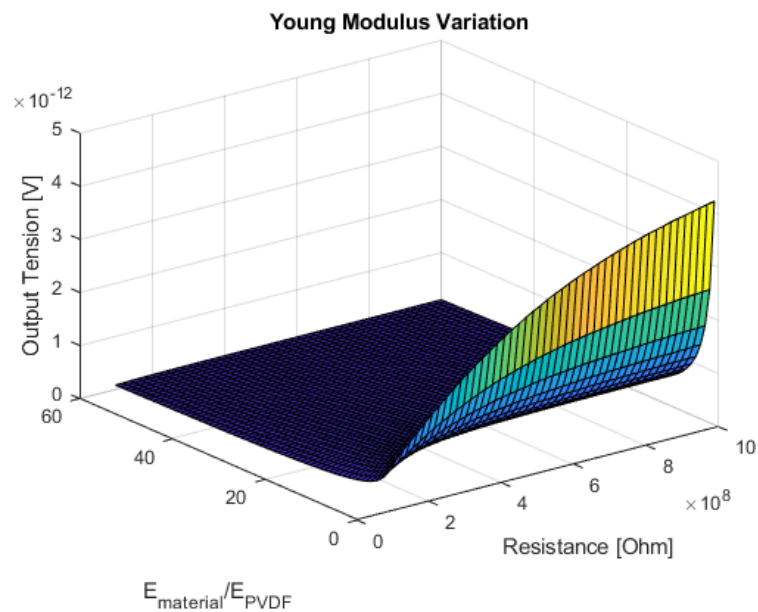


Fig. 17: Young modulus- variation, 3D analysis, **X-axis**= resistance variation, **Y-axis**= $\frac{E_{\text{material}}}{E_{\text{PVDF}}}$, **Z-axis**= piezoelectric voltage output

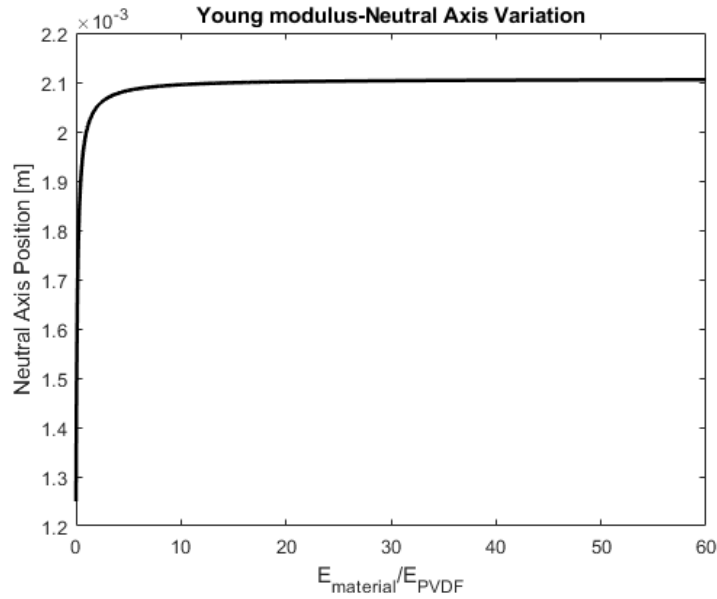


Figure 18: Young modulus-neutral axis variation, 2D analysis, **X-axis** = $\frac{E_{\text{material}}}{E_{\text{PVDF}}}$, **Y-axis** = neutral axis position.

As regard the First Frequency of the normal modes, is possible to see that it increase with the young modulus of the base material. That means that harder is the material and higher is the first frequency of the normal modes.

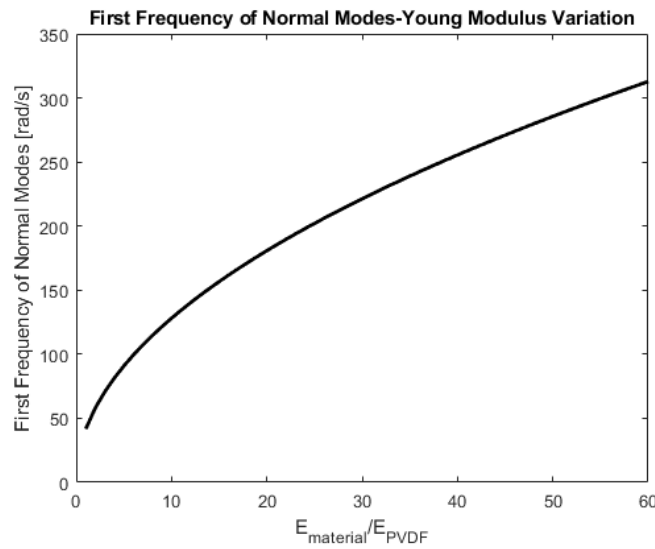


Figure 19: Young modulus-frequency of normal modes variation, 2D analysis, first frequency of normal modes variation with a fixed resistance of $8e8$ [Ohm], **X-axis** = $\frac{E_{\text{material}}}{E_{\text{PVDF}}}$, **Y-axis** = first frequency of normal modes

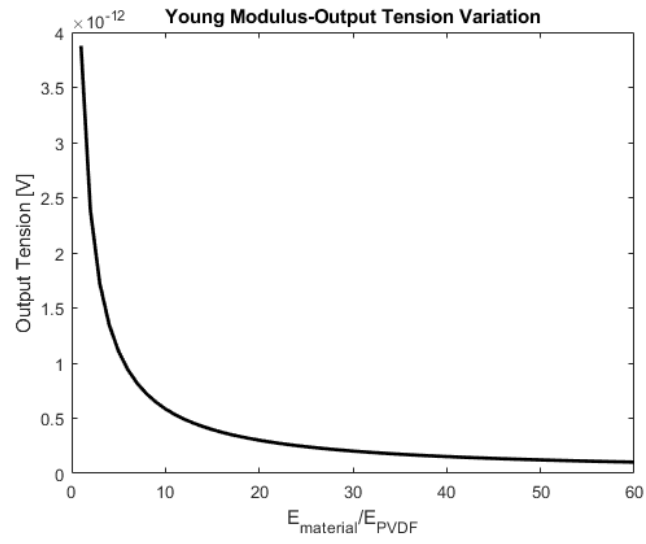


Figure 20: Young modulus-voltage output variation with fixed resistance of $8e8$ [Ohm] detail, 2D analysis, **X-axis:** $\frac{E_{material}}{E_{PVDF}}$, **Y-axis:** piezoelectric material output tension

CHAPTER 6

CONCLUSION AND FUTURE WORK

6.1 Summary

Piezoelectric materials were always used as sensors and actuators because of their cost and the capability to convert mechanical stress into electric charge and vice versa. Over the last few years, many research types were made to apply this kind of material in wireless technology and low-power electronic devices.

The objective of this work was to develop a model that allows to explore the effect of the position of a piezoelectric material embedded into a cantilever beam related to the harvesting power, to understand the behavior of this smart structure under a base vibration, and to find the optimum output voltage harvesting power. To this scope, the development of this work was done with three steps. The initial stages of the work were spent in the study of the problem and with the analysis of the free vibration response of the structure. Once the first part of the work was done, A dynamic analysis of the structure was made and then confronted with an FEA model's simulation to validate the results. To this end, many FEA models were created to find the most accurate one.

Conclusively, A parametric analysis was run in order to obtain the different harvested power output related to the various configurations of the smart structure.

In light of the results obtained from this work, the optimal configuration for a beam with an embedded piezoelectric material and any material as base material presents the PVDF layer on the top/bottom edge of the beam with a length equal to $\frac{1}{2}$ of the total length of the structure and a smart material thickness of the 65% of the total height of the beam. Regarding the Elastic material study, the harder the base material is, and less is the output voltage harvested from the Piezoelectric layer so, it is suggested to use this sensor with a soft base material to harvest the maximum power from the smart material.

For instance, for the beam configuration studied in this dissertation, the optimal output voltage is obtained from a PVDF position on the top or the bottom of the beam, a layer length of 0.16 m (out of the total length of 0.32 m), and thickness of 0.0026 m (out of the 0.004 m of the total thickness).

Table 5: Optimal configuration for a beam with a PVDF sensor embedded

Parameter	Optimal Configuration
First part of the beam length	Half of the total length of the beam
Second part of the beam length	Half of the total length of the beam
Embedded piezoelectric thickness	65% of the total thickness of the beam
Base material thickness	35% of the total thickness of the

Resistance of the equivalent circuit	beam 8e8 [ohm]
---	-------------------

6.2 Future Work

There are several possibilities of work for the future to further this work. The first step in the future should be to build the beam and test the framework that has been developed. After that, it can be extended the framework to a higher-order beam theory. Furthermore, a non-linear analytical analysis model could be studied, and the results could be compared with physical experimentations. Another extension could be adding a crack propagation theory, test this structure in a simulation environment, and then confront the results. Finally, the same work with a Timoshenko theory could be developed to overcome some of the limitations that rule the slender beam.

APPENDIX A

HAMILTONIAN EQUATION

$$\begin{aligned}
\int_0^L H &= \int_0^L H_1 + H_2 \\
&= \int_l^L +\rho A_{eff2} \left(-\frac{\partial^2 w_{rel2}(x_2, t)}{\partial t^2} - \frac{\partial^2 w_{rel1}(l, t)}{\partial t^2} - \frac{\partial^2 w_b(t)}{\partial t^2} - x_2 \frac{\partial^2 w_{rel1}'(l, t)}{\partial x_1^2} \right. \\
&\quad \left. - E_2 I_{eff2} \frac{\partial^4 w_{rel2}(x_2, t)}{\partial x^4} \right) \delta w_{rel2}(x_2, t) \\
&\quad + \int_l^L +\rho A_{eff2} \left(-\frac{\partial^2 w_{rel1}(l, t)}{\partial t^2} - \frac{\partial^2 w_{rel2}(x_2, t)}{\partial t^2} - \frac{\partial^2 w_b(t)}{\partial t^2} \right. \\
&\quad \left. - x_2 \frac{\partial w_{rel1}'(l, t)}{\partial x_1} \right) \delta w_{rel1}(l, t) + \left[E I_{eff1} \frac{\partial^3 w_{rel1}(x_1, t)}{\partial x^3} \delta w_{rel1} \right]_0^l \\
&\quad + \int_l^L +\rho A_{eff2} \left(-\frac{\partial^2 w_{rel2}(x_2, t)}{\partial t^2} - \frac{\partial^2 w_{rel1}(l, t)}{\partial t^2} - \frac{\partial^2 w_b(t)}{\partial t^2} \right. \\
&\quad \left. - x_2 \frac{\partial^2 w_1'(l, t)}{\partial x_1^2} \right) x_2 \delta w_{rel1}'(l, t) \\
&\quad + \left[\left(-E I_{eff1} \frac{\partial^2 w_{rel1}(x_1, t)}{\partial x^2} + \theta V(t) \right) \delta \left(\frac{\partial w_{rel1}}{\partial x} \right) \right]_0^l \\
&\quad + \left[E_2 I_{eff2} \frac{\partial^3 w_{rel2}(x_2, t)}{\partial x^3} \delta w_{rel2}(x_2, t) \right]_0^L \\
&\quad - \left[E_2 I_{eff} \frac{\partial^2 w_{rel2}(x_2, t)}{\partial x^2} \delta \left(\frac{\partial w_{rel2}(x_2, t)}{\partial x} \right) \right]_0^L \\
&\quad + \int_0^l \left[-\rho A_{eff1} \left(\frac{\partial^2 w_{rel1}(x_1, t)}{\partial t^2} + \frac{\partial^2 w_b(t)}{\partial t^2} \right) \right. \\
&\quad \left. - E I_{eff1} \frac{\partial^4 w_{rel1}(x_1, t)}{\partial x^4} \right] \delta w_{rel1}(x_1, t) dx + \int_0^l e_{31} H_p \left(\frac{\partial^2 w_{rel1}}{\partial x^2} \right) \delta V(t) dx \\
&\quad + \frac{1}{2} \int_0^l \varepsilon_{33} \frac{b}{(h_2)} V^2(t) dx \} + Q \delta V
\end{aligned}$$

APPENDIX B

COEFFICIENTS OF CONSTRAINTS EQUATIONS

The matrix showed in equation (3.48) denote a system of five equations in 4 unknown variables C_1, D_1, D_2, D_3 while, to solve the dynamic problem, it was used the system showed in (B.1), it is basically the same system showed in (3.48) but it has one more variable: V . The determinants of these two matrix give the characteristic equations.

$$\begin{bmatrix} A_{11} & A_{12} & A_{13} & A_{14} & A_{15} & A_{16} \\ A_{21} & A_{22} & A_{23} & A_{24} & A_{25} & A_{26} \\ A_{31} & A_{32} & A_{33} & A_{34} & A_{35} & A_{36} \\ A_{41} & A_{42} & A_{43} & A_{44} & A_{45} & A_{46} \\ A_{51} & A_{52} & A_{53} & A_{54} & A_{55} & A_{56} \\ A_{61} & A_{62} & A_{63} & A_{64} & A_{65} & A_{66} \end{bmatrix} \begin{Bmatrix} C_1 \\ C_2 \\ D_1 \\ D_2 \\ D_3 \\ V \end{Bmatrix} = \begin{Bmatrix} 0 \\ 0 \\ 0 \\ 0 \\ 0 \\ 0 \end{Bmatrix} \quad (\text{B.1})$$

Where the coefficients A_{ij} are:

$$A_{11} = \cosh(\beta_2 L) \sin(\beta_1 l) - \cosh(\beta_2 L) \sinh(\beta_1 l) \quad (\text{B.2})$$

$$A_{12} = \cos(\beta_1 l) \cosh(\beta_2 L) - \cosh(\beta_1 l) \cosh(\beta_2 L) \quad (\text{B.3})$$

$$A_{13} = -\sin(\beta_2 L) \quad (\text{B.4})$$

$$A_{14} = -\cos(\beta_2 L) - \cosh(\beta_2 L) \quad (\text{B.5})$$

$$A_{15} = \sinh(\beta_2 L) \quad (\text{B.6})$$

$$A_{16} = 0 \quad (\text{B.7})$$

$$A_{21} = \sin(\beta_1 l) \sinh(\beta_2 L) - \sinh(\beta_1 l) \sinh(\beta_2 L) \quad (\text{B.8})$$

$$A_{22} = \cos(\beta_1 l) \sinh(\beta_2 L) - \cosh(\beta_1 l) \sinh(\beta_2 L) \quad (\text{B.9})$$

$$A_{23} = -\cos(\beta_2 L) \quad (\text{B.10})$$

$$A_{24} = \sin(\beta_2 L) - \sinh(\beta_2 L) \quad (\text{B.11})$$

$$A_{25} = \cosh(\beta_2 L) \quad (\text{B.12})$$

$$A_{26} = 0 \quad (\text{B.13})$$

$$\begin{aligned} A_{31} = & \frac{\rho A_{eff2} \omega^2}{\beta_2^2} \{ \sin(\beta_1 l) [1 - \cosh(\beta_2 L)] - \sinh(\beta_1 l) [1 - \cosh(\beta_2 L)] \} \\ & + EI_{eff1} \beta_1^2 [\sin(\beta_1 l) + \sinh(\beta_1 l)] \\ & + \frac{\rho A_{eff2} \omega^2 L}{\beta_2} \sinh(\beta_2 L) [\sin(\beta_1 l) - \sinh(\beta_1 l)] \end{aligned} \quad (\text{B.14})$$

$$A_{32} = \frac{\rho A_{eff2} \omega^2}{\beta_2^2} \{ \cos(\beta_1 l) [1 - \cosh(\beta_2 L)] - \cosh(\beta_1 l) [1 - \cosh(\beta_2 L)] \} \\ + EI_{eff1} \beta_1^2 [\cos(\beta_1 l) + \cosh(\beta_1 l)] \\ + \frac{\rho A_{eff2} \omega^2 L}{\beta_2} \sinh(\beta_2 L) [\cos(\beta_1 l) - \cosh(\beta_1 l)] \quad (B.15)$$

$$A_{33} = -\frac{\rho A_{eff2} \omega^2 L}{\beta_2} \cos(\beta_2 L) + \frac{\rho A_{eff2} \omega^2}{\beta_2^2} \sin(\beta_2 L) \quad (B.16)$$

$$A_{34} = \frac{\rho A_{eff2} \omega^2}{\beta_2^2} [\cos(\beta_2 L) + \cosh(\beta_2 L) - 2] + \frac{\rho A_{eff2} \omega^2 L}{\beta_2} [\sin(\beta_2 L) - \sinh(\beta_2 L)] \quad (B.17)$$

$$A_{35} = \frac{\rho A_{eff2} \omega^2}{\beta_2^2} [\cos(\beta_2 L) + \cosh(\beta_2 L) - 2] + \frac{\rho A_{eff2} \omega^2 L}{\beta_2} [\sin(\beta_2 L) - \sinh(\beta_2 L)] \quad (B.18)$$

$$A_{36} = 0 \quad (B.19)$$

$$A_{41} = -EI_{eff1} \beta_1^3 [\cos(\beta_1 l) + \cosh(\beta_1 l)] + \frac{\rho A_{eff2} \omega^2}{\beta_2} \sinh(\beta_2 L) [\sin(\beta_1 l) - \sinh(\beta_1 l)] \quad (B.20)$$

$$A_{42} = EI_{eff1} \beta_1^3 [\sin(\beta_1 l) - \sinh(\beta_1 l)] + \frac{\rho A_{eff2} \omega^2}{\beta_2} \sinh(\beta_2 L) [\cos(\beta_1 l) - \cosh(\beta_1 l)] \quad (B.21)$$

$$A_{43} = \frac{\rho A_{eff2} \omega^2}{\beta_2} [1 - \cos(\beta_2 L)] \quad (B.22)$$

$$A_{44} = \frac{\rho A_{eff2} \omega^2}{\beta_2} [\sin(\beta_2 L) - \sinh(\beta_2 L)] \quad (B.23)$$

$$A_{45} = -\frac{\rho A_{eff2} \omega^2}{\beta_2} [1 - \cosh(\beta_2 L)] \quad (B.24)$$

$$A_{46} = -\theta \quad (B.25)$$

$$A_{51} = \beta_1 \cosh(\beta_1 l) - \beta_1 \cos(\beta_1 l) \quad (B.26)$$

$$A_{52} = \beta_1 \sin(\beta_1 l) + \beta_1 \sinh(\beta_1 l) \quad (B.27)$$

$$A_{53} = \beta_2 \quad (B.28)$$

$$A_{54} = 0 \quad (B.29)$$

$$A_{55} = \beta_2 \quad (B.30)$$

$$A_{56} = 0 \quad (B.31)$$

$$A_{61} = \frac{\theta R}{\beta_1} [-\sin(\beta_1 l) - \sinh(\beta_1 l)] \quad (B.32)$$

$$A_{62} = \frac{\theta R}{\beta_1} [-\cos(\beta_1 l) - \cosh(\beta_1 l)] \quad (B.33)$$

$$A_{63} = 0 \quad (B.34)$$

$$A_{64} = 0 \quad (B.35)$$

$$A_{65} = 0 \tag{B.36}$$

$$A_{66} = 1 \tag{B.37}$$

APPENDIX C

CLAMP DESIGN PROCESS

Motivation

In order to reduce the walking problem that affects the UAM machine's welding and increase the percentage of good welding, some improvement to the UAM machine was necessary.

As shown in Fig., the clamp equipped to the UAM machine provides two types of force. An axial force that prevents the movement and the slipping of the tape during the welding, and a horizontal pull that follows the tape's elongation caused by the plastic deformation of the aluminum under the normal force and the transversal vibrations provided by the sonotrode.

In the first part of the developing process, it was considered to substitute the clamp machine device of the UAM machine with one tool that clamps the tape with a normal force only, reduces the tape walking problem (that often affected our weldings), and increases the welding performances. After different designs and tests, it was realized that substitute the clamp of the machine would be too ambitious, so we opted, after the third design, to use the pulling and clamp effect that the machine provides but improve in some way to obtain better weldings and, with the last design, it was designed a guide for the tape to reduce the walking problem and maintain the welding path straight. Unfortunately, the last design was never built and tested.

First Design

The first clamp design consisted of a structure of 10" long, 2" wide and 1" thick with several aligned holes of 0.28" of diameter where it is possible to set the screws which are going to put an axial force on the tape and provide the clamping effect. Two bolts on the device's edge are necessary to hold the clamp to the baseplate and receive contrast the opposite force received from the clamping effect. There are several advantages with this structure, but the most important is that this clamp can move. Hence, it is possible to clamp near the end of the welding so reduce the length of the aluminum that it should be placed on the base plate, saving material, and reducing the possibility of walking (it was noticed by colleagues and me that longer is the welding path and the tape and more are the chances of walking of the foil) . The main disadvantage of this tool is the few degrees of freedom. There are only certain places where it is possible to set the foil, so there are fewer possibilities to use the welding plate efficiently.

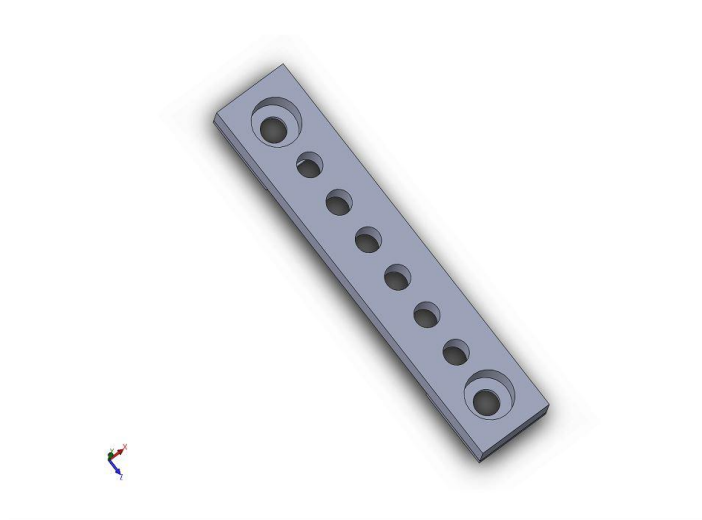


Figure 21: First Design Model, Upper view

Second Design

The second design was an improvement of the first one. This new structure, shown in 22 solved two main problems, the few degrees of freedom of the first design and the high degree of inflection of the system (while the clamp effect was provided) due to the normal force that the screw receives from the clamp function. Four parts form this clamp, a bottom and an upper part of 10" long, 2" wide, a screwdriver structure of 0.28" of internal diameter, 0.32" of external diameter with two cylinders on the side, and two supports of different height in order to be adaptable to the extra height of the welding. The screw was inserted into the screwdriver in order to obtain the normal force that needed to fix the tape on the plate, with this support the upper and bottom parts of this structure. Have a buttonhole, so it was possible to shift the setscrew driver in the right position for the different weldings and efficiently use the welding plate. This clamp allows the creation of different structures with many shapes and gives the freedom to create complex structures without concerning the welding or foils' position.

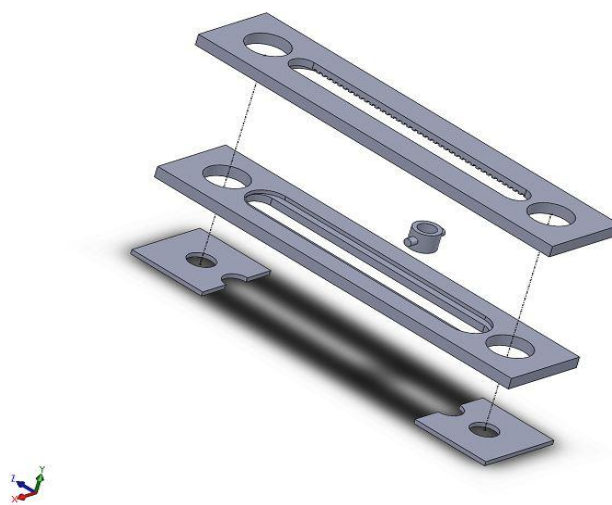


Figure 22: Second design model, upper view

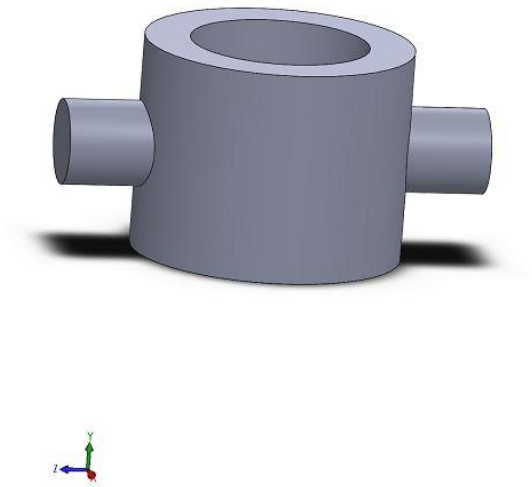


Figure 23: Second design model, screw driver detail

This structure's main problems were the crack initiation on the junction of the set screwdriver and the possibility that the screwdriver could move under a transverse vibration. After many weldings, there were a higher possibility that a crack could appear on the junction between the two cylinders and the screwdriver. This issue brings us to the new clamp next design

Third Design

With the third design, it was decided to improve the second one's structure, adding some features. The whole clamp has the same dimension exception made for the setscrew driver. Instead of the cylinder setscrew driver shape, a rectangular parallelepiped shape and four smaller rectangular parallelepipeds were used on the edges. It was chosen this design because many sites were made on the clamp's upper part, where the four extremities can be inserted and fix the set screwdriver after the clamp function. With this new feature, the setscrew driver couldn't move under the vibrations forces caused by the sonotrode, so the tape was fixed in a better way.

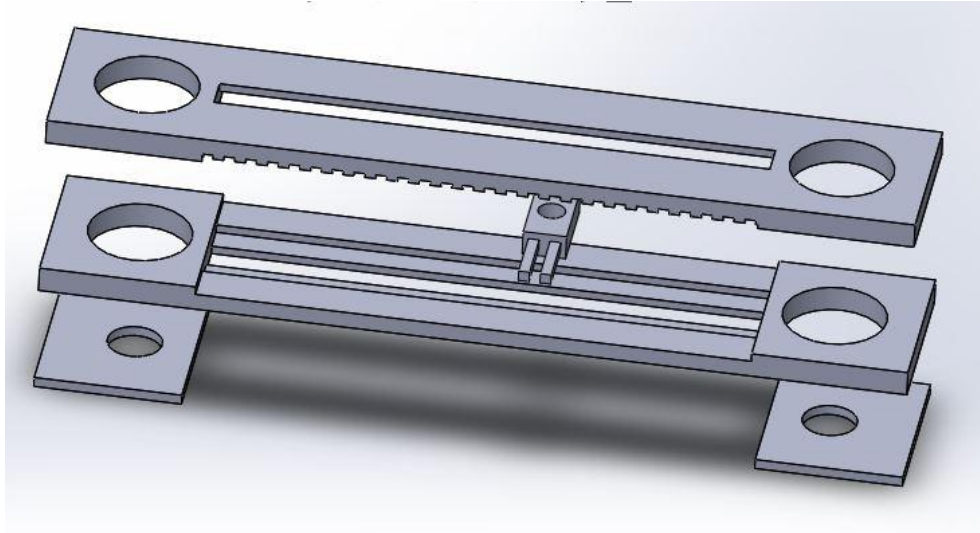


Figure 24: Third design model, upper view

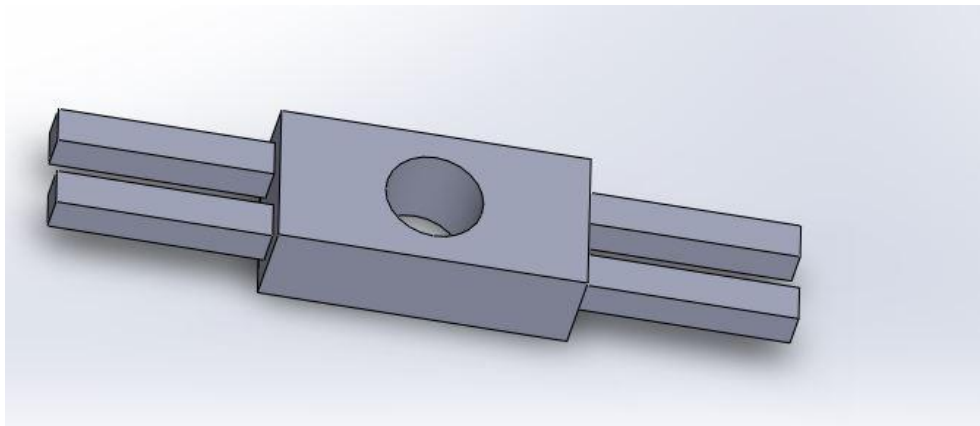


Figure 25: Third design model, screw driver detail

Third Design: Fabrication And Test Results

The prototype of this structure was made by PLA and printed with the Ultimaker printer. This material fitted the requirements of durability and strength perfectly because of his excellent properties with a flexural strength of 103 MPa, impact strength Izod tested to 5.1 kJ/m², and a hardness of 83 Shore D. The creation of this structure took 14 hours but, after them, the test was run immediately.

In Fig. 26 is shown the clamp while was working on the plate. The screw fixed the tape perfectly, but the normal force resulting from this action was enough to bend the upper clamp part as is possible to see in Fig. 27. This bending didn't affect the welding, but this problem could affect the

lifetime of the structure. So an improvement with the material was necessary, and an Al3003 clamp was thought for this purpose.

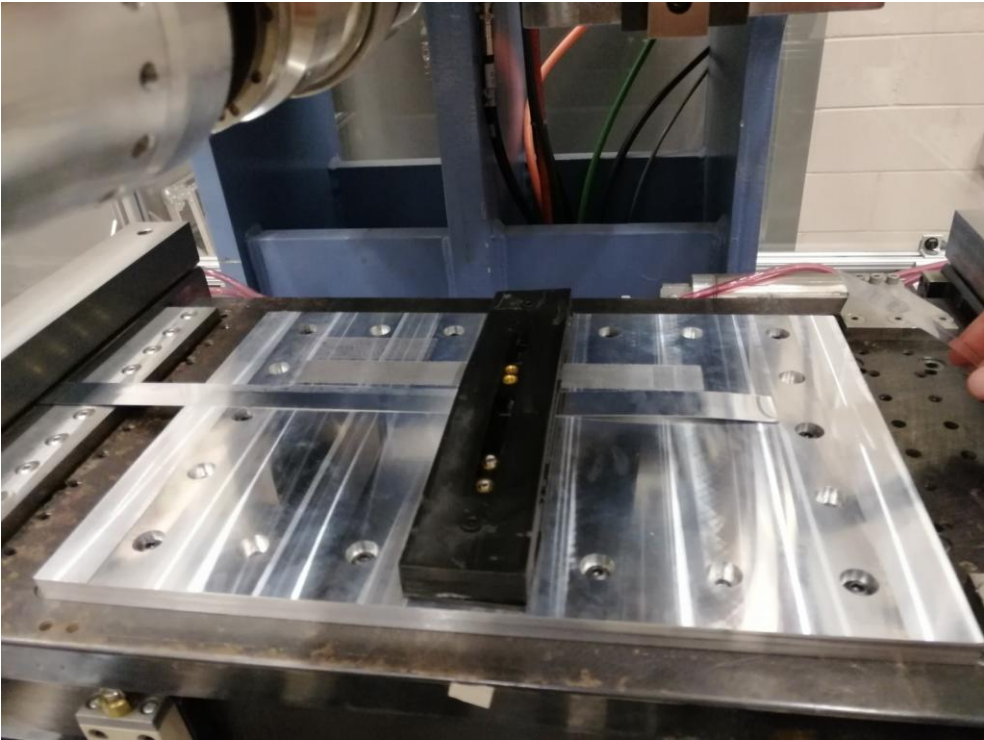


Figure 26: Third design model test, upper view



Figure 27: Third design clamp model bending, lateral view

Many tests were run with this structure, and many things were noticed. From Fig. 28 is possible to see the first problem of the clasper, it doesn't follow the elongation of the tape (because the screw provides only a normal force), so there is an excess of material after the end of the welding. In addition, the screws used to fix the tape affected the baseplate leaving a little damaging it.

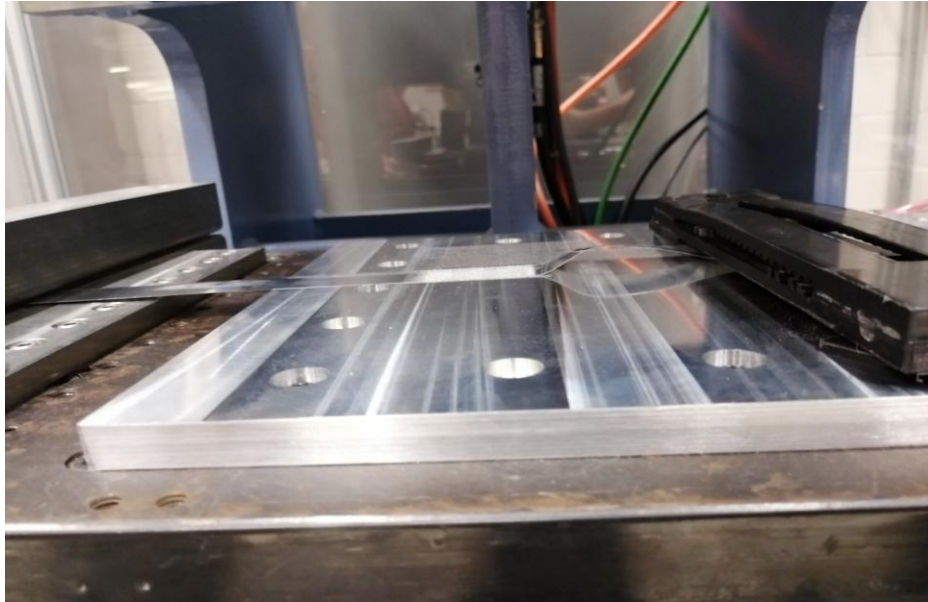


Figure 28: First test result, lateral view

From Fig. 28 it is easy to notice that setting the screw, the tape received a torsional momentum force. Indeed Fig. 29 and Fig. 30 show a different elongation on the left side of the tape and a little walk of the tape.

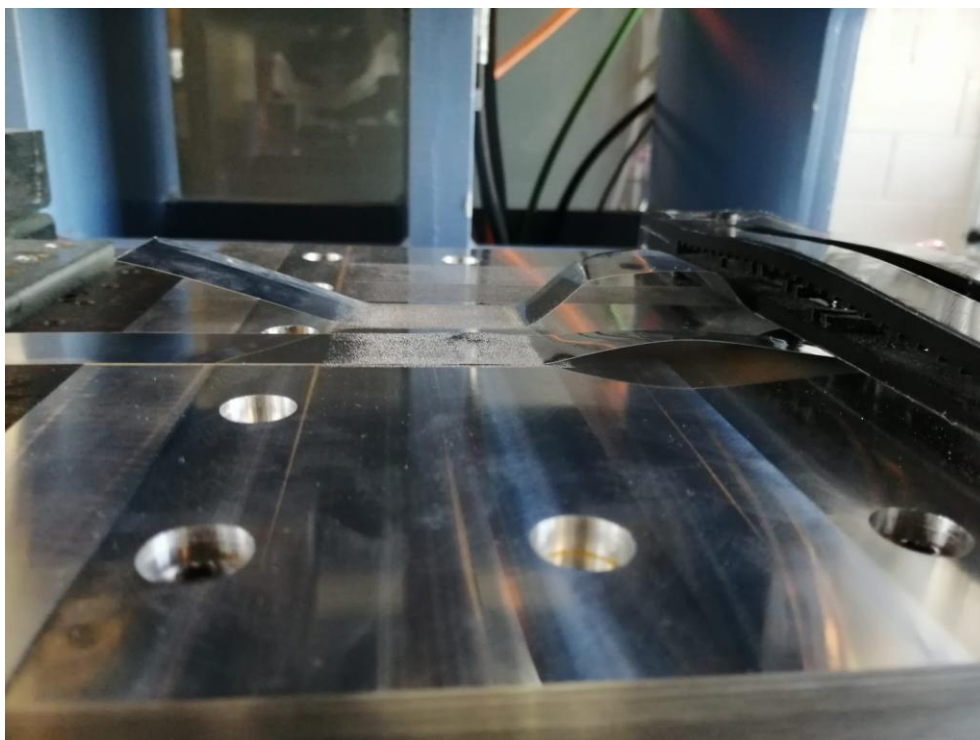


Figure 29: Second test result, lateral view

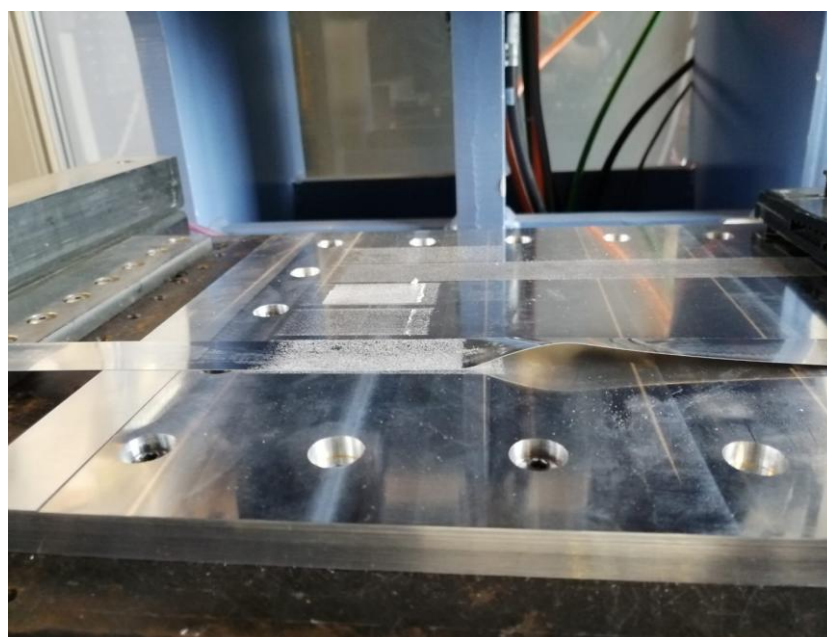


Figure 30: Second test result, detail



Figure 31: Welding parameters, UAM machine display

After these considerations, it was decided to create a new design without screws that provided also a pulling horizontal force to follow the tape elongation.

Fourth Design

With the fourth design, the approach of this problem was completely changed. In light of the issue that showed up during the third design test, It was decided to use a device that allows the clamp to follow the elongation of the tape, fix the Aluminum foil inside itself, and didn't affect the plate.

With this clamp, a cylinder, and two blocks on his edge to support it was used. Inside the blocks, It was made room for the two sides of the main cylinder (in order to allow the contact between them), and two springs (that gave the rotation and the tension needed to follow the aluminum foil's elongation). As regards the cylinder, as is shown in Fig. 33 , holes for the screws, on the top of it, and a rectangular hole along all his length was made.

To make the tool work, it was necessary to turn the cylinder, obtain the torque momentum, then insert the tape in the cylinder's hole and fix it, setting the screw in the correct position. All the functions that were needed were achieved with this clamp: fix the aluminum foil, and follow the tape's elongation. After many calculi, it was realized that the main problem of this structure was the spring. It should give a huge momentum, but, to obtain this force, a spring with a diameter that doesn't follow our requirements was needed, so the idea of spring was abandoned, and a new designed was thought

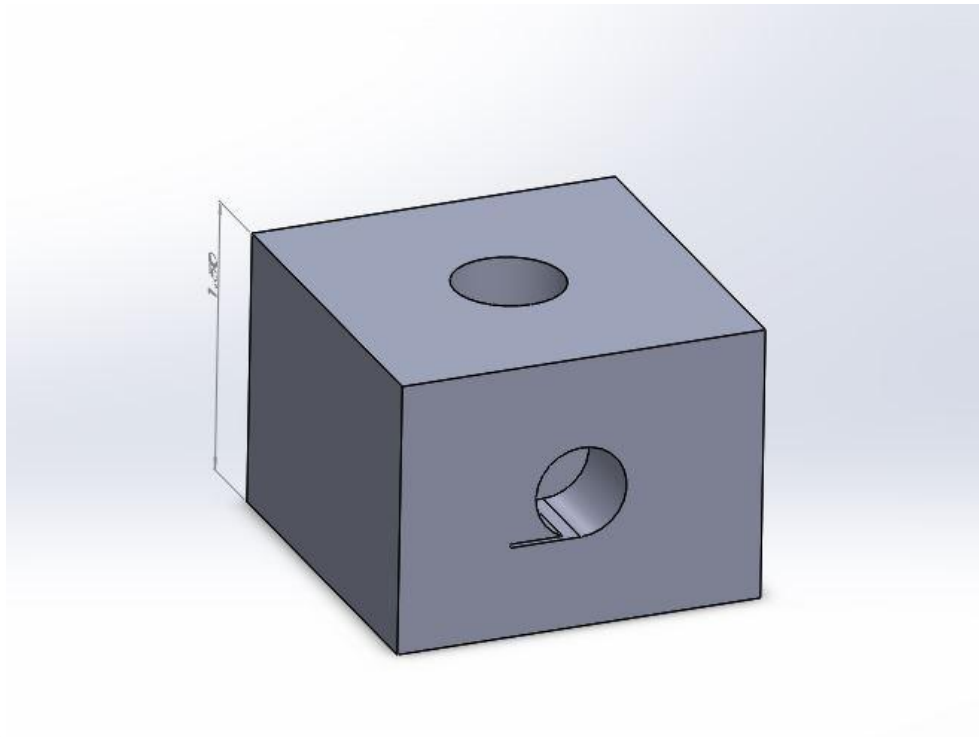


Figure 32: Fourth design, cylinder support, lateral view, detail



Figure 33: Fourth Design, Cylinder, lateral view detail

Fifth Design

Due to the previous design dimension, it was decided to obtain the clamp and the pulling function effects from the machine's clamp device and use the clamp as an additional tool that provides an angle to the tape. With this angle, it is possible to create structures and weldings without the issue that other systems on the baseplate could cause a failure of the welding, tape walking, or damage to the tape during the welding phase. Damages of different entities can occur because the tape could be placed above other structures (as the standard procedure says, in order to use the baseplate more efficiently). During the elongation phase, the aluminum foil caused by the sonotrode action could be affected by the friction received by the upper part of the other weldings or other sharp parts. As Fig. shows, the new clamp is made by two cylinders of 1" each made in PLA, two bearings of 0.5" each made by softer plastic, and two parallelepipeds rectangular shaped as bases. The Functioning of this device is easy to be understood. The tape is placed on the top of the upper cylinder to obtain the needed angle. The tape is then rolled on the lower cylinder (the effects of this action are that the tape is parallel to the machine's clamp to maximize the pulling and the fixing function provided by the machine clamp). Another advantage of this tool is that the friction received from the cylinders' surfaces helps the tape don't slip under the machine's clamp device.

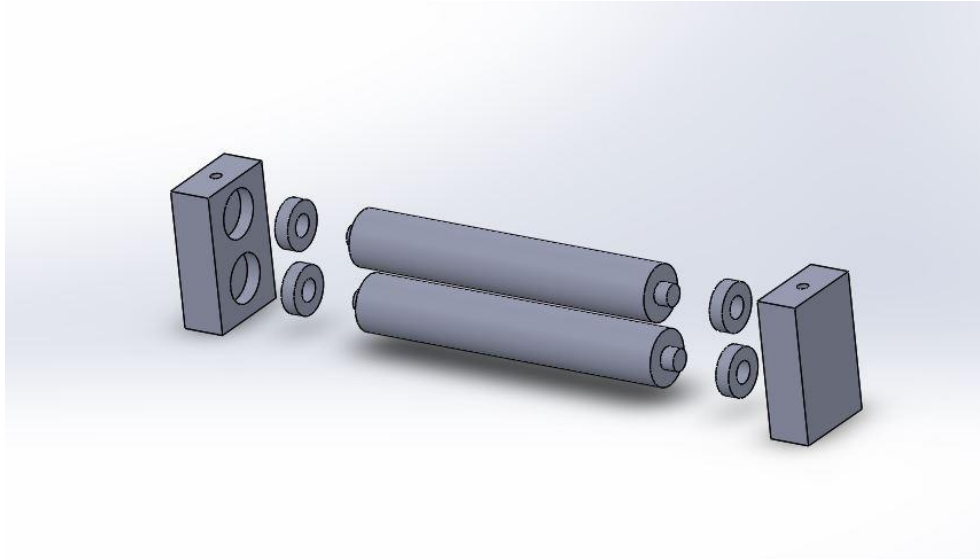


Figure 34: Fifth Design, upper view

The clamp's most remarkable effect was adding friction that the tape received from the two cylinders that helped to reduce the walking problem, but it wasn't enough to significantly overcome this issue. After this consideration came the last idea for a clamp that could improve the machine welding.

Sixth Design

In light of all the previous designs, tests, and considerations, it was noticed that the machine's clamp was enough to our goal. The use of the machine's clamp was the right way, so it was decided to add a new feature to it, a guide. The third design was modified by changing the screwdriver with a guide made by two straight pieces of 2" long and 0.15" wide made by PLA. The clamp and these two pieces should be fixed close to the welding end on the aluminum tape edges. In this way, the aluminum foil's elongation, obtained during the welding phase, is guided. This simple solution decreases the walking problem hugely. By the way, this tool was never prototyped and tested.

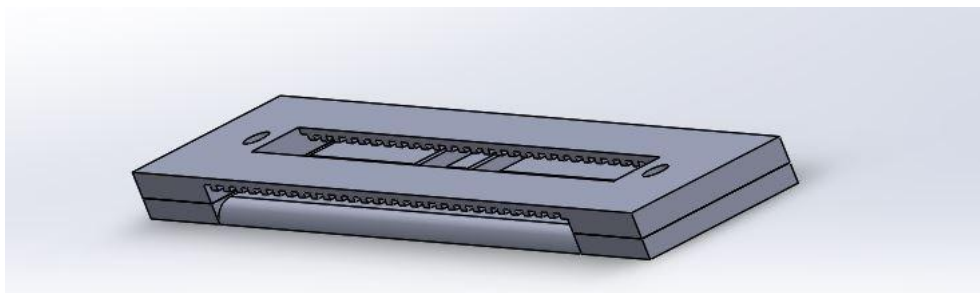


Figure 35: Sixth Design

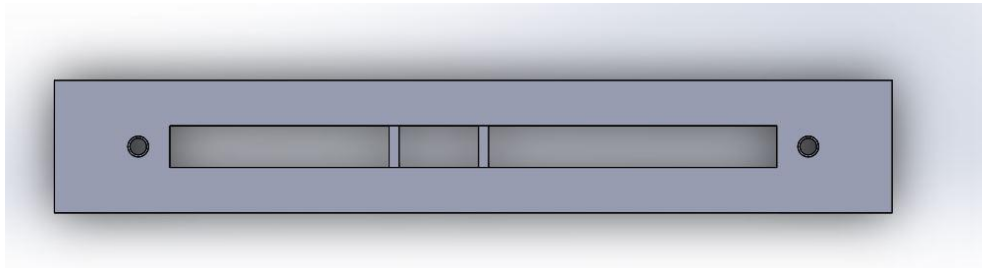


Figure 36: Sixth Design, upper view

BIBLIOGRAPHY

- [1] A. Abdelkefi, F. N. (2011). An Energy Harvester Using Piezoelectric Cantilever Beams Undergoing Coupled Bending-Torsion Vibrations. *Smart Materials and Structures* , 115007.
- [2] A.Haddow, A. B. (1984). Theoretical and experimental Study of Modal Interaction in a Two-Degree-of-Freedom Structure. *Journal of Sound and Vibration* , 451-473.
- [3] A.V. Shirinov, W. S. (2008). Pressure Sensor from a PVDF Film. *Sensor and Actuators* , 48-55.
- [4] Aldraihem, O. S. (1997). Realistic Determination of the Optimal Size and Location of Piezoelectric Actuators/Sensor. *Proceedings of the 1997 IEE International Conference on Control Applications* , 435-440.
- [5] Crawley, E. F. (1987). Structures, Use of Piezoelectric Actuators as Elements of Intelligent. *AIAA Journal* , 1373-1385.
- [6] D.C.D Oguamanam, J. S. (1998). Vibration of Arbitrarily Oriented Two-Member Open Frames with Tip Mass. *Journal of Sound and Vibration* , 651-669.
- [7] F.Geirgiades, J. W. (2012). Linear Modal Analysis Of I-Shaped Beam Structures Parametric Studies. *Journal of Physic: Conference Series* , 012006.
- [8] Franco Correia, V. M. (2000). Modelling and Design of Adaptive Composite Structures. *Computer methods in applide mechanics and engineering* , 325-346.
- [9] Gibert, F. D. (2018, March 19). Exact Dynamics of an Angle-Shaped Resonator for Energy Scavenging Applications. *SPIE 10595, Active and Passive Smart Structures and Integrated system XII* , 1-19.
- [10] Gugliotta, A. (2002). *Elementi Finiti: Parte II*. Torino: Otto Editore.
- [11] H.A. Soldano, G. P. (2004). Estimation of Electric Charge Output for Piezoelectric Energy Harvesting. *Strain* , 49-58.
- [12] Henry A. Soldano, D. J. (2004, May). A Review of Power Harvesting From Vibration using Piezoelectric Materials. *The Shock and vibration Digest* , 197-205.
- [13] Inman, A. E. (2008). A Distributed Parameter Electromechanical Model For Cantilevered Piezoelectri Energy Harvester. *Journal of Vibration and Acoustic* , 041002-041002-15.
- [14] Ip, K.-H. P.-C. (2001). Optimal Configuration of a Piezoelectric Patch for Vibration Control of Isotropic Rectangular Smart Plates. *Smart Materials and Structures* , 395-403.
- [15] J.li, M. S.-V. (2015). Exploring the Mechanic Strength of Additively Manufactured Metal Structures With Embedded Electrical Materials. *Material & Science Engineering* , 474-481.

- [16] Johannes Riemenschneider, R. M. (2017). Integration of Actuators by Additive Layer Manufacturing. *ASME 2017 Conference on Smart Materials, Adaptive Structures and Intelligent System* .
- [17] Meirovitch, L. (2001). *Foundamentals of Vibrations*. Boston: McGraw-Hill.
- [18] Moheimani, S. a. (1999). Considerations on Placement of Piezoelectric Actuators That are Used in Structural Vibration Control. *Proceedings of the 38th IEE Conference on Decision and Control* , 1118-1123.
- [19] Molter, A. d. (2019). An Optimality Criteria-Based method for the Simultaneous Optimization of the structural Design and Placement of Piezoelectric Actuators. *Structural and Multidisciplinary Optimization* , 1125-1141.
- [20] Paolo Mazzoldi, M. N. (2010). *Elementi di Fisica: Meccanica, Termodinamica*. Padova: EdiSES.
- [21] Quek, S. W. (2016). Vibration Control of Composite Plates via Optimal Placement of Piezoelectric Patches. *Journal of Intelligent Material System and Structures* , 229-245.
- [22] Rao, S. S. (2007). *Vibration of Continuous Systems*. Hoboken, New Jersey: John Wiley & sons, INC.
- [23] Tiersten, H. (1967-68). Hamilton's Principle for Linear Piezoelectric Media. *Proceedings of the IEEE* , 1523-1524.
- [24] Wang, Q. W. (2000). Optimal Placement and Size of Piezoelectric Patches on Beams from the Controllability Perspective. *Smart Materials Structure* , 558-567.
- [25] Young Ting, S. A.-W. (2016). Design and Characterization of One-Layer PVDF Thin film Film for a 3D force. *Sensor and Actuators A: Physical* , 129-137.